

# 000 001 002 003 004 005 006 007 008 009 010 011 012 013 014 015 016 017 018 019 020 021 022 023 024 025 026 027 028 029 030 031 032 033 034 035 036 037 038 039 040 041 042 043 044 045 046 047 048 049 050 051 052 053 LEARNING TO SEGMENT FOR VEHICLE ROUTING PROBLEMS

Anonymous authors

Paper under double-blind review

## ABSTRACT

Iterative heuristics are widely recognized as state-of-the-art for Vehicle Routing Problems (VRPs). In this work, we exploit a critical observation: a large portion of the solution remains stable, i.e., unchanged across search iterations, causing redundant computations, especially for large-scale VRPs with long subtours. To address this, we pioneer the formal study of the First-Segment-Then-Aggregate (FSTA) decomposition technique to accelerate iterative solvers. FSTA preserves stable solution segments during the search, aggregates nodes within each segment into fixed hypernodes, and focuses the search only on unstable portions. Yet, a key challenge lies in identifying which segments should be aggregated. To this end, we introduce Learning-to-Segment (L2Seg), a novel neural framework to intelligently differentiate potentially stable and unstable portions for FSTA decomposition. We present three L2Seg variants: non-autoregressive (globally comprehensive but locally indiscriminate), autoregressive (locally refined but globally deficient), and their synergy. Empirical results on CVRP and VRPTW show that L2Seg accelerates state-of-the-art solvers by 2x to 7x. We further provide in-depth analysis showing why synergy achieves the best performance. Notably, L2Seg is compatible with traditional, learning-based, and hybrid solvers, while supporting various VRPs.

## 1 INTRODUCTION

Vehicle Routing Problems (VRPs) have profound applications such as in logistics and ride-hailing, driving advances in combinatorial optimization (Laporte, 2009). As NP-hard problems, they are typically tackled with heuristics approximately. Neural Combinatorial Optimization (NCO) (Kool et al., 2018; Bengio et al., 2021; Luo et al., 2024; Berto et al., 2023) has recently introduced machine learning into VRP solving, enabling data-driven decision-making with minimal domain knowledge while matching and even surpassing the performance of meticulously designed heuristics such as Lin-Kernighan-Helsgaun (LKH)(Helsgaun, 2017) and Hybrid Genetic Search (HGS)(Vidal, 2022).

Generally, state-of-the-art VRP solvers predominantly rely on iterative search to refine solutions through local search (e.g., ruin and repair). However, as noted in Section 3, a significant portion of edges *stabilize*<sup>1</sup>, or their presence in the solution stops changing between iterations, as the search progresses, despite repeated local search. For example, inner edges of neighboring subtours may remain fixed while only boundary edges undergo frequent combinatorial changes. Intuitively, such stability can be inferred from customer spatial distribution and the solution properties through end-to-end learning. Yet, existing solvers overlook such opportunities, leading to redundant computations that hinder their scalability and efficiency, especially in large-scale VRPs with long subtours.

Motivated by this critical observation, we study how learning to identify such *segments* can accelerate iterative search solvers, a perspective yet to be explored to the best of our knowledge. To this end, we formalize a **First-Segment-Then-Aggregate (FSTA)** decomposition framework, which identifies stable segments in a VRP solution and then aggregates them as fixed (one or two) hypernodes with combined attributes (e.g., total demand, min/max time windows). This not only decomposes the original large problem into more tractable subproblems but also significantly accelerates the search

<sup>1</sup>Specifically, we define *stable edges* as those that consistently remain in the solution across consecutive solver invocations, where each invocation performs a full optimization round (multiple local search operations) within a fixed budget to return a locally optimal solution (see Appendix A.1 for formal definitions).

054 by leveraging iterative local search to strategically focus on unstable portions. We further show that  
 055 FSTA preserves solution equivalence and is broadly applicable to VRPs with diverse constraints.  
 056

057 To identify unstable portions for FSTA decomposition, we then introduce **Learning-to-Segment**  
 058 (**L2Seg**), a novel learning-guided framework that leverages deep models to intelligently differentiate  
 059 potentially stable and unstable portions, allowing dynamic decomposition for accelerated local search.  
 060 Realizing this, however, is nontrivial: it involves a large combinatorial decision space requiring  
 061 accurate segment grouping, and demands modeling complex interdependencies among predicted  
 062 edges, constraints, spatial distribution, solution structures, and both node and edge features.  
 063

064 To address these challenges, L2Seg proposes encoder-decoder-styled neural models. The encoder  
 065 integrates graph-level and route-level features using attention and graph neural networks, gener-  
 066 ating node embeddings that guide edge re-optimization predictions. L2Seg offers three decoders:  
 067 (1) L2Seg-NAR (Non-Autoregressive): which features one-shot fast global prediction; (2) L2Seg-AR  
 068 (Autoregressive), which enjoys sequential dependency modeling for high-precision local predictions;  
 069 and (3) L2Seg-SYN (Synergized), which balances the strengths of both NAR and AR. Notably, this  
 070 represents a pioneering work that explores the joint decision-making between AR and NAR models  
 071 in neural combinatorial optimization. Our L2Seg models are trained via a weighted cross-entropy  
 072 loss on datasets labeled using a lookahead procedure: edge stability is classified based on whether its  
 073 presence in the solution was changed during iterative re-optimization.  
 074

075 Extensive experiments on large-scale CVRPs and VRPTWs show that L2Seg accelerates backbone  
 076 heuristics by 2x to 7x, enabling them to outperform state-of-the-art classic, neural, and hybrid  
 077 baselines, while generalizing well across different customer distributions and problem sizes. Notably,  
 078 L2Seg exhibits strong flexibility in enhancing various solvers, including the classic LKH-3 ([Helsgaun, 2017](#))  
 079 solver, other orthogonal Large Neighborhood Search (LNS) methods ([Shaw, 1998](#)), and  
 080 learning-guided decomposition method Learning-to-Delegate (L2D) ([Li et al., 2021](#)). We further  
 081 analyze the synergy between AR and NAR models, showing their combination achieves the best  
 082 performance by integrating NAR’s global comprehension with AR’s local precision.  
 083

084 Our contributions are: (1) We make a critical yet underexplored insight that stable segments persist  
 085 across search iterations in large-scale VRPs, causing redundant computations; (2) We formally study  
 086 and theoretically prove the properties and applicabilities of First-Segment-Then-Aggregate (FSTA)  
 087 for various VRPs; (3) We develop Learning-to-Segment (L2Seg), a learning-guided framework with  
 088 bespoke network architecture, training, and inference for segment identification; (4) We propose  
 089 autoregressive, non-autoregressive, and their synergistic deep models, pioneering the first-of-its-kind  
 090 study in NCO; (5) L2Seg consistently accelerates state-of-the-art iterative VRP solvers by 2x to 7x,  
 091 boosting both classic and learning-based solvers, including other decomposition frameworks.  
 092

## 093 2 RELATED WORKS

094 **VRP Solvers.** Classical VRP solvers include exact methods with guarantees ([Baldacci et al., 2012](#))  
 095 and practical heuristics ([Helsgaun, 2017](#)). Recently, machine learning has been applied to combi-  
 096 natorial optimization, either end-to-end ([Kool et al., 2018; Kwon et al., 2020; Fang et al., 2024;](#)  
 097 [Geisler et al., 2022; Gao et al., 2024; Drakulic et al., 2023; Wang et al., 2024; Min et al., 2023; Li](#)  
 098 [et al., 2023a](#)) or learning-guided to unite data-driven insights into human solvers ([Li et al., 2021; Lu](#)  
 099 [et al., 2023; Huang et al., 2024; 2023; Hottung et al., 2025](#)). For VRPs, the former could yield  
 100 competitive performance to classic methods ([Drakulic et al., 2023; Luo et al., 2023](#)), while the latter  
 101 often achieve state-of-the-art performance ([Zheng et al., 2024](#)). Among these, most effective VRP  
 102 solvers rely on iterative search, including classic heuristics such as HGS ([Vidal, 2022](#)), LNS ([Shaw,](#)  
 103 [1998](#) and LKH ([Helsgaun, 2017](#)); neural solvers that learn local search ([Ma et al., 2021; 2023; Kim](#)  
 104 [et al., 2023; Hottung and Tierney, 2022; Ma et al., 2022](#)); neural constructive solvers integrated with  
 105 search components ([Luo et al., 2023; Hottung et al., 2022; Kim et al., 2021; Sun and Yang, 2023;](#)  
 106 [Chalumeau et al., 2023; Kim et al., 2024; Qiu et al., 2022](#)); and hybrid learning-guided methods like  
 107 L2D ([Li et al., 2021](#)). However, both handcrafted and neural iterative search solvers overlook the  
 108 redundant computations identified in this paper, particularly in large-scale VRPs.  
 109

110 **Decomposition for Large-scale VRPs.** Scalability in VRP solvers often relies on effective decom-  
 111 position that operates on solutions partially ([Santini et al., 2023](#)). This includes hand-crafted heuristics,  
 112 such as LNS ([Shaw, 1998](#)) and evolutionary algorithms ([Helsgaun, 2017](#)), as well as learning-based  
 113

108 methods such as sub-tour grouping (Zong et al., 2022), problem variant reduction (Hou et al., 2023),  
 109 action space decomposition (Drakulic et al., 2023; Luo et al., 2023; Zhou et al., 2025a), spatial-  
 110 based decomposition (Zheng et al., 2024; Zhou et al., 2025b; Pan et al., 2025), and **hypergraphs**  
 111 **decomposition** (Li et al., 2025; Fu et al., 2023). In this paper, we present FSTA and L2seg, a fresh<sup>2</sup>.  
 112 learning-based decomposition framework that automatically detects unstable edges and aggregates  
 113 stable segments. Notably, L2Seg holds potential to enhance other decomposition methods, such as  
 114 LNS (Shaw, 1998) and L2D (Li et al., 2021). While another related work (Morabit et al., 2024)  
 115 explores segment stability for re-optimization in a specific dynamic CVRP setting, our work addresses  
 116 a different problem, i.e., identifying stable segments across search steps to accelerate iterative solvers.  
 117 And we formally analyze the solution equivalence of FSTA across broader VRP variants. Moreover,  
 118 L2Seg uniquely designs and integrates three novel deep learning models (AR, NAR, and synergized)  
 119 to guide FSTA decomposition during search.

120 **AR and NAR Models.** In NCO, NAR models make global predictions like edge heatmaps (Sun  
 121 and Yang, 2023; Li et al., 2023b). However, they struggle to model complex interdependencies,  
 122 particularly VRP constraints. In contrast, AR models make sequential predictions, e.g., node by node  
 123 selection in construction solvers (e.g., Luo et al. (2023)). AR offers stronger modeling capacity but  
 124 might overlook global structure. Recent NCO works combine AR and NAR models in divide-and-  
 125 conquer frameworks, with NAR for problem splitting and AR for solving (Zheng et al., 2024; Hou  
 126 et al., 2023; Ye et al., 2024). We are the first to leverage their complementary strengths for joint  
 127 decision-making, enabling more effective identification of unstable segments in FSTA decomposition.

### 3 FIRST-SEGMENT-THEN-AGGREGATE (FSTA)

#### 3.1 VEHICLE ROUTING PROBLEMS (VRPs)

132 VRPs aim to minimize total travel costs (often distance or travel time)  
 133 while serving a set of customers under constraints. Formally, a **VRP**  
 134 **instance  $P$**  is defined on a graph  $G = (V, E)$ , where each node  $x_i \in V$   
 135 represents a customer and each edge  $e_{i,j} \in E$  represents traveling from  
 136  $x_i$  to  $x_j$  and is associated with a travel cost. For Capacitated VRP  
 137 (CVRP), vehicles of capacity  $C$  start and end at a depot node  $x_0$ . The  
 138 sum of the demands  $d_i$  on any route must not exceed  $C$ , and each  
 139 customer should be served exactly once. For VRP with Time Windows  
 140 (VRPTW), each customer is additionally associated with a service time  
 141  $s_i$  and a time window  $[t_i^l, t_i^u]$  within which service must begin. See  
 142 Appendix A for the formal definitions of CVRP and VRPTW.

#### 3.2 FSTA DECOMPOSITION

145 Figure 1 depicts that iterative search solvers perform **redundant searches**, reoptimizing only a small  
 146 portion while many edges remain unchanged, especially in large subtours with high capacity  $C$ .  
 147 Inspired by Morabit et al. (2024), we formally study the decomposition technique, First-Segment-  
 148 Then-Aggregate (FSTA), for accelerating iterative search solvers. As shown in the top of Figure 2,  
 149 **FSTA segments the VRP solutions by identifying unstable portions, and then groups the stable**  
 150 **segments into hypernodes.** We thus expect more efficient re-optimization on the reduced problems  
 151 with smaller size. More visualization of FSTA is provided in Appendix B.1.

152 **Segment Definition.** Denote the solution (set of routes) of a CVRP as  $\mathcal{R} = \{R^1, R^2, \dots\}$ , and each  
 153 route as  $R^i = (x_0 \rightarrow x_1^i \rightarrow x_2^i \rightarrow \dots \rightarrow x_0) \in \mathcal{R}$ , where the first and the last nodes in  $R^i$  are  
 154 the depot. A segment consists of some consecutive nodes within a route. We denote the segment  
 155 containing the  $j^{\text{th}}$  to  $k^{\text{th}}$  nodes of route  $i$  as  $S_{j,k}^i = (x_j^i \rightarrow \dots \rightarrow x_k^i)$ . An aggregated segment  $\tilde{S}_{j,k}^i$   
 156 uses one hypernode ( $\tilde{S}_{j,k}^i = \{\tilde{x}_{j,k}^i\}$ ) or two hypernodes ( $\tilde{S}_{j,k}^i = \{\tilde{x}_j^i, \tilde{x}_k^i\}$ ) with aggregated attributes  
 157 (e.g. the demand of  $\tilde{x}_{j,k}^i$  equals to  $d_j^i + \dots + d_k^i$ ) to represent the non-aggregated segment  $S_{j,k}^i$ .

159 **FSTA Solution Update.** After identifying unstable edges  $\{e_{j_1}^i, e_{j_2}^i, \dots\}$  in each route (which will be  
 160 addressed in Section 4), where each  $e_j^i$  denotes the edge starting from the  $j^{\text{th}}$  node in route  $R^i$ , we

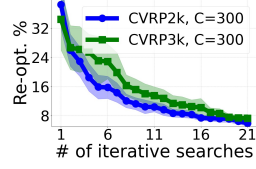


Figure 1: Percentage of re-optimized edges during iterative search using LKH-3 on 100 CVRP instances. Most edges remain unchanged, suggesting redundant calculations.

<sup>2</sup>A detailed comparison with representative decomposition methods is provided in Appendix C.1

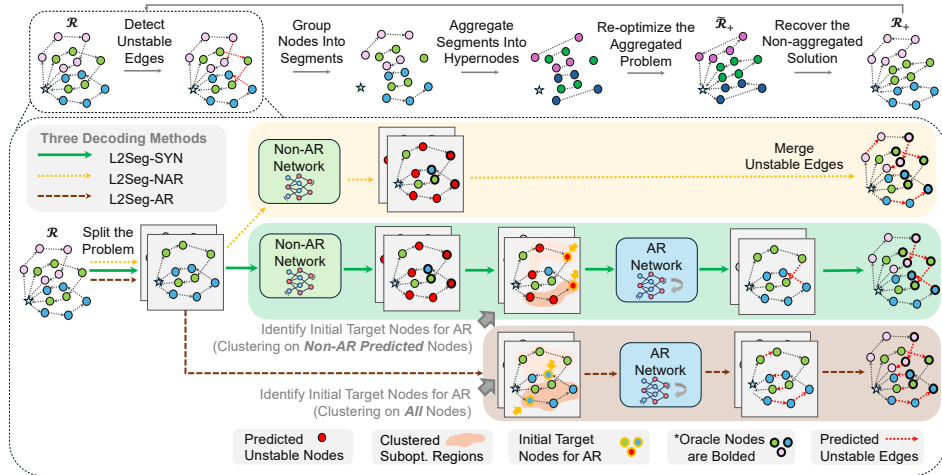


Figure 2: The overview of our FSTA decomposition framework (top) and the three proposed L2Seg models (bottom). L2Seg-SYN employs a four-step synergized approach: (1) problem decomposition into subproblems, (2) unstable nodes detection globally via NAR decoding, (3) clustering of NAR-predicted nodes to localize unstable regions and select initial target nodes, and (4) refining unstable edge predictions locally via AR decoding starting from these identified initial target nodes.

break these edges and group the remaining stable edges into segments. To preserve a valid depot, edges connecting to the depot are included in the unstable edge set. After unstable edges are removed, each route  $R^i$  is then decomposed into multiple disjoint segments  $\{x_0, S_{1,j_1}^i, S_{j_1,j_2}^i, \dots\}$ , where  $x_0$  is depot. Each segment  $S_{j,k}^i$  is then aggregated into one or two hypernodes  $\tilde{S}_{j,k}^i$ , leading to a reduced problem  $\tilde{P}$ . We then obtain the corresponding solution  $\tilde{\mathcal{R}}$  for such reduced problem, where for each  $\tilde{R}^i \in \tilde{\mathcal{R}}$ , we have  $\tilde{R}^i = (x_0 \rightarrow \tilde{S}_{1,j_1}^i \rightarrow \tilde{S}_{j_1,j_2}^i \dots \rightarrow x_0)$ . With fewer nodes than the original problem  $P$ , re-optimization with a backbone solver becomes more efficient, which is analyzed and confirmed in Appendix B.1. After re-optimization, we obtain a new solution  $\tilde{\mathcal{R}}_+$  for the reduced problem  $\tilde{P}$ , which is then recovered into a solution  $\mathcal{R}_+$  for the original problem  $P$  by expanding each hypernode(s) back into its original segment of nodes. This relies on our monotonicity theorem, which guarantees that an improved solution in  $\tilde{P}$  maps to an improved solution in  $P$ .

**Theoretical Analysis.** We establish a theorem proving FSTA’s feasibility and monotonicity across multiple VRP variants (e.g. CVRP, VRPTW, VRPB, and 1-VRPPD), with the proof in Appendix B.2.

**Theorem (Feasibility)** If the aggregated solution  $\tilde{\mathcal{R}}_+$  is feasible to the aggregated problem, then  $\mathcal{R}_+$  is also feasible to the original, non-aggregated problem.

**Theorem (Monotonicity).** If two feasible aggregated solutions  $\tilde{\mathcal{R}}_+^1$  and  $\tilde{\mathcal{R}}_+^2$  satisfy  $f(\tilde{\mathcal{R}}_+^1) \leq f(\tilde{\mathcal{R}}_+^2)$ , where  $f(\cdot)$  denotes the objective function (total travel cost), their corresponding original solutions also preserve this order:  $f(\mathcal{R}_+^1) \leq f(\mathcal{R}_+^2)$ .

## 4 LEARNING TO SEGMENT (L2SEG)

We introduce **Learning to Segment (L2Seg)**, a neural framework for predicting unstable edges to guide FSTA. We consider two paradigms: 1) Non-autoregressive (NAR) and 2) Autoregressive (AR) models. *NAR models* offer global predictions with an efficient single forward pass. However, they lack conditional modeling to accurately capture local dependencies. For example, when one edge is unstable, nearby edges often show instability but not all, but NAR models may fail to distinguish them and mark all neighboring edges as unstable. On the other hand, *AR models* can more natively capture local dependencies. Yet, they may miss the crucial global structure. For example, when unstable edges are distributed across distant regions, AR models may struggle to recognize and model these broader patterns. Our approach offers three variants as shown in Figure 2: non-autoregressive (L2Seg-NAR), autoregressive (L2Seg-AR), and a synergized combination of both (L2Seg-SYN).

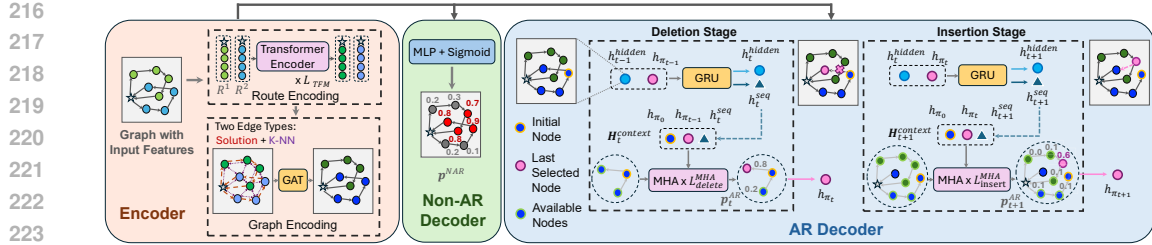


Figure 3: Architecture of L2Seg: encoder (left), NAR decoder (center), and AR decoder (right). NAR predicts unstable nodes for associated edges. AR uses a two-stage process, where the insertion bridges the deletion stage to accurately detect unstable edges locally, akin to the local search behavior.

#### 4.1 NEURAL ARCHITECTURE

The autoregressive and non-autoregressive models of L2Seg share the same encoder structure. Next, we first describe the encoder, and then the two decoder architectures.

**Input Feature Design.** We propose enhanced input features for L2Seg to better distinguish unstable and stable edges (see Appendix B.1 for intuitions). Key features include node angularity relative to the depot and node internality, where the latter measures the proportion of nearest nodes within the same route. We consider two edge types: edges in the current solution  $\mathcal{R}$  and edges connecting each node to their  $k$ -nearest neighbors. Appendix C.2 provides a detailed feature description.

**Encoder.** Given node features  $\mathbf{X} = (\mathbf{x}_0, \mathbf{x}_1, \dots)$  and edge features  $\mathbf{E} = \{\mathbf{e}_{0,1}, \mathbf{e}_{0,2}, \dots\}$ , we compute the initial node embedding as  $\mathbf{h}_i^{\text{init}} = \text{Concat}(\mathbf{h}_i^{\text{MLP}}, \mathbf{h}_i^{\text{POS}}) \in \mathbb{R}^{2d_h}$ , where  $\mathbf{h}_i^{\text{MLP}}$  and  $\mathbf{h}_i^{\text{POS}}$  are obtained by passing  $\mathbf{x}_i$  through a multilayer perceptron (MLP) and an absolute position encoder (Vaswani, 2017), respectively. Next, we process the embeddings using  $L_{\text{TFM}}$  Transformer layers (Vaswani, 2017) with masks to prevent computation between nodes in different routes:  $\mathbf{h}_i^{\text{TFM}} = \text{TFM}(\mathbf{h}_i^{\text{init}}) \in \mathbb{R}^{d_h}$ . This step encodes local structural information from the current solution. Finally, we compute the node embeddings  $\mathbf{H}^{\text{GNN}} = \{\mathbf{h}_i^{\text{GNN}} \in \mathbb{R}^{d_h} \mid i = 0, \dots, |V|\}$  leveraging the global graph information by using  $L_{\text{GNN}}$  layers of a Graph Attention Network (GAT) (Veličković et al., 2017), where  $\mathbf{H}^{\text{GNN}} = \text{GNN}(\mathbf{H}^{\text{TFM}}, \mathbf{E})$ .

**Non-Autoregressive Decoder.** It uses an MLP with a sigmoid function to decode the probability  $\mathbf{p}^{\text{NAR}}$  of each node being unstable globally in one shot, so as to identify associated unstable edges:

$$\mathbf{p}^{\text{NAR}} = \text{MLP}_{\text{NAR}}(\mathbf{H}^{\text{GNN}}) \quad (1)$$

**Autoregressive Decoder.** The autoregressive decoder models unstable edge interdependence by generating them sequentially as  $a = \{x_{\pi_0}, x_{\pi_1}, \dots\}$ . Following classical local search where  $k$  removed edges are reconnected via  $k$  new insertions (Funke et al., 2005), the sequence alternates between deletion (identifying unstable edges) and insertion (introducing pseudo-edges that bridge to the next unstable edge), terminating at  $x_{\text{end}}$ . **Note that the "insertion" stage is designed to model dependencies between consecutive unstable edges rather than actually "insert" edges into the solution.** Formally, denote the set of edges within the current solution as  $E_{\mathcal{R}}$ . The decoding alternates between: (1) **Deletion** ( $t = 2k$ ): Selects an unstable edge  $e_{\pi_{2k}, \pi_{2k+1}} \in E_{\mathcal{R}}$  based on a target node, which is either initialized at the first step (see Section 4.3) or the one obtained from the previous insertion step; one of the two edges connected to this node in the current solution is then selected as unstable (more than two candidates may exist if the node is the depot); **importantly, this edge is only marked as unstable, not immediately removed from the solution;** and (2) **Insertion** ( $t = 2k + 1$ ): Selects an new edge  $e_{\pi_{2k+1}, \pi_{2k+2}} \notin E_{\mathcal{R}}$  that links to the endpoint of the last unstable edge removed, exploring  $O(|V|)$  potential candidates to serve as a bridge to the next unstable target node (next unstable region). From  $a$ , we then identify the set of removed edges as the unstable edges, i.e.,  $E_{\text{unstable}} = \{e_{\pi_0, \pi_1}, e_{\pi_2, \pi_3}, \dots\}$ . Both stages employ two principal modules: Gated Recurrent Units (GRUs) (Chung et al., 2014) to encode sequence context, and multi-head attention (MHA) (Vaswani, 2017) for node selection. The GRU's initial hidden state is the average of all node embeddings:  $\mathbf{h}_0^{\text{hidden}} = \frac{1}{|V|} \sum_{i=0}^{|V|} \mathbf{h}_i^{\text{GNN}}$ . At step  $t$ , the sequence embedding is updated by  $\mathbf{h}_t^{\text{seq}} = \text{GRU}(\mathbf{h}_{t-1}^{\text{hidden}}, \mathbf{h}_{\pi_{t-1}}^{\text{GNN}})$ , and the context embedding is

270 formed by concatenating the embeddings of the initial node, the previous node, and the new sequence  
 271 embedding:  $\mathbf{H}_t^{\text{context}} = \text{Concat}(\mathbf{h}_{\pi_0}^{\text{GNN}}, \mathbf{h}_{\pi_{t-1}}^{\text{GNN}}, \mathbf{h}_t^{\text{seq}})$ .  
 272

273 Inspired by the decoder design in LEHD (Luo et al., 2023), we use two distinct MHA modules with  
 274  $L^{\text{MHA}}$  layers, to decode  $x_{\pi_t}$ . Specifically, considering the size of the action space (at most 2 for  
 275 deletion and  $O(|V|)$  for insertion), we utilize a shallow decoder ( $L_{\text{delete}}^{\text{MHA}} = 1$ ) during the deletion  
 276 stage and a deeper decoder ( $L_{\text{insert}}^{\text{MHA}} = 4$ ) during the insertion stage. Let  $\mathbf{H}_t^a \subseteq \mathbf{H}^{\text{GNN}}$  denote the set  
 277 of available nodes at step  $t$ . During the insertion stage, we also incorporate an additional candidate  
 278  $\mathbf{h}^{\text{end}} = \alpha \mathbf{h}_{\pi_0}^{\text{GNN}} + (1 - \alpha) \frac{1}{|V|} \sum_{i=0}^{|V|} \mathbf{h}_i^{\text{GNN}}$ , where  $\alpha$  is a learnable parameter, to indicate termination  
 279 of decoding, providing the AR model flexibility to determine the number of unstable edges. Formally,  
 280 the decoding at step  $t$  is given as follows; note that the first 3 dimensions of  $\mathbf{H}^{(L^{\text{MHA}})}$  corresponds to  
 281 context embeddings  $\mathbf{H}_t^{\text{context}}$  and hence are masked from selection:  
 282

$$\begin{aligned} \mathbf{H}^{(0)} &= \text{Concat}(\mathbf{H}_t^{\text{context}}, \mathbf{H}_t^a), \\ \mathbf{H}^{(l)} &= \text{MHA}(\mathbf{H}^{(l-1)}), \\ u_i &= \begin{cases} (W_q \mathbf{h}^c)^T W_k \mathbf{h}_i^{(L^{\text{MHA}})} / \sqrt{d_h}, & \text{if } i > 3, \\ -\infty, & \text{O.W.} \end{cases} \end{aligned} \quad (2)$$

290 where  $1 \leq l \leq L^{\text{MHA}}$ ,  $W_q$  and  $W_k$  are learnable matrices, and  $\mathbf{h}^c \in \mathbb{R}^{6d_h}$  concatenates the first three  
 291 columns of  $\mathbf{H}^{(0)}$  and  $\mathbf{H}^{(L^{\text{MHA}})}$  along the last axis. The node  $x_{\pi_t}$  is sampled from  $\mathbf{p}_t^{\text{AR}} = \text{softmax}(\mathbf{u})$ .  
 292

## 4.2 TRAINING

293 We employ iterative solvers as look-ahead heuristics  
 294 to detect unstable edges. We utilize imitation learning  
 295 to train L2Seg models to replicate the behavior of the  
 296 look-ahead heuristics.

307 **Dataset Construction.** Let the edges in  $\mathcal{R}$  be  $E_{\mathcal{R}}$ , and  
 308 nodes indicated by edge set  $E$  be  $V_E$ . Given  $P$  with  
 309 current solution  $\mathcal{R}$ , we first employ an iterative solver  $\mathcal{S}$  to  
 310 refine  $\mathcal{R}$  and obtain  $\mathcal{R}_+$ . We then collect differing edges  
 311 as  $\mathcal{R}$  and  $\mathcal{R}_+$  as  $E_{\text{diff}} = (E_{\mathcal{R}} \setminus E_{\mathcal{R}_+}) \cup (E_{\mathcal{R}_+} \setminus E_{\mathcal{R}})$  (in-  
 312 cluding both the deleted and newly inserted edges). Next,  
 313 we identify the set of unstable nodes  $V_{\text{unstable}} = V_{E_{\text{diff}}}$ ,  
 314 i.e., the set of nodes that are end points to some edge in  
 315  $E_{\text{diff}}$ . We empirically observe that solution refinement  
 316 typically takes place between two adjacent routes. **For the NAR model**, we construct a dataset with binary  
 317 labels. Each problem-label pair consists of a decomposed  
 318 problem containing two adjacent routes and binary labels  
 319 indicating whether each node is unstable (1) or  
 320 stable (0). Formally, a node  $x$  is labeled 1 if  $x \in V_{\text{unstable}}$ .  
 321 **For the AR model**, we construct labels as node se-  
 322 quences preserving local dependencies among unstable  
 323 edges. Nodes without local dependencies are naturally excluded through connected component  
 324 partitioning. We obtain connected components  $\mathcal{K}$  induced by  $E_{\text{diff}}$  and select those spanning at  
 325 most two routes, denoted  $\mathcal{K}_{\text{TR}}$ . For each  $K \in \mathcal{K}_{\text{TR}}$  containing nodes from routes  $R_i$  and  $R_j$ , we  
 326 form a subproblem  $P_K$  with solution  $\mathcal{R}_K = \{R_i, R_j\}$ . From each component  $K$  (dashed circles  
 327 in Figure 4), we extract a node sequence  $y_K = \{x_{\pi_0}, x_{\pi_1}, \dots, x_{\pi_m}, x_{\text{end}}\}$  by alternating between  
 328 edge deletion and insertion operations (shown in Figure 4, second row). These problem-label pairs  
 329 ( $P_K, y_K$ ) constitute **the AR model** training data.

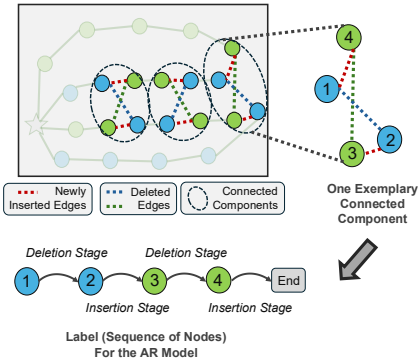


Figure 4: Training data construction for the AR model. Re-optimization reveals deleted edges (blue/green dashed) and inserted edges (red dashed) forming connected components (circles). For each component, depth-first search generates node sequences alternating between deletion and insertion operations, terminated by an end token as the AR model’s training label.

324 **Loss Function.** To balance labels, we use weighted binary cross-entropy for the NAR model ( $w_{\text{pos}} >$   
 325 1) and weighted cross-entropy for the AR model to balance the two stages ( $w_{\text{insert}} > w_{\text{delete}}$ ).  
 326

$$327 \quad L_{\text{NAR}}(\mathbf{p}^{\text{NAR}}, y^{ij}) = - \sum_{y_{x_k} \in y^{ij}} w_{\text{pos}} y_{x_k} \log(p_k^{\text{NAR}}) + (1 - y_{x_k}) \log(1 - p_k^{\text{NAR}})$$

$$328 \quad L_{\text{AR}}(\mathbf{p}^{\text{AR}}, y_K) = - \sum_{x_{\pi_{2k}} \in y_K} w_{\text{insert}} \log(p_{\pi_{2k}}^{\text{AR}}) - \sum_{x_{\pi_{2k+1}} \in y_K} w_{\text{delect}} \log(p_{\pi_{2k+1}}^{\text{AR}}).$$

$$329$$

$$330$$

$$331$$

332 **4.3 INFERENCE**

333 We describe the synergized inference that combines the benefits of global structural awareness from  
 334 NAR with the local precision from AR, followed by two variants using only NAR or AR.  
 335

336 **Synergized Prediction (L2Seg-SYN).** L2Seg-SYN’s inference pipeline for detecting unstable edges  
 337 consists of four steps: (1) problem decomposition, (2) global unstable node detection via NAR  
 338 decoding, (3) representative initial node identification for AR decoding based on NAR predictions,  
 339 and (4) local unstable edge detection using AR decoding.  
 340

341 Given a problem  $P$  with solution  $\mathcal{R}$ , we partition  $P$  into approximately  $|\mathcal{R}|$  subproblems,  $\mathcal{P}_{\text{TR}}$ , by  
 342 grouping nodes from all two adjacent sub-tour pairs. For each subproblem in  $\mathcal{P}_{\text{TR}}$ , the NAR model  
 343 predicts unstable nodes as  $\hat{y}_{\text{NAR}} = \{x_i \mid p_i^{\text{NAR}} \geq \eta\}$ , where  $\eta$  is a predefined threshold. We then  
 344 refine unstable edge detection with the AR model within regions identified by the NAR prediction.  
 345 To reduce redundant decoding efforts on neighboring unstable nodes, we first group unstable nodes  
 346 into  $n_{\text{KMEANS}}$  clusters using the  $K$ -means algorithm, and select the node with the highest  $p_i^{\text{NAR}}$   
 347 within each cluster as the starting point for AR decoding. The AR model then detects unstable edges  
 348 based on these initial nodes. Finally, we aggregate unstable edges from all subproblems in  $\mathcal{P}_{\text{TR}}$  as  
 349 the final unstable edge set for  $P$  given the current solution  $\mathcal{R}$ .  
 350

351 **Non-Autoregressive Prediction (L2Seg-NAR).** L2Seg-NAR uses only the NAR model for predictions.  
 352 It identifies unstable nodes and marks all connected edges as unstable.  
 353

354 **Autoregressive Prediction (L2Seg-AR).** L2Seg-AR exclusively uses the AR model. Instead of using  
 355 the NAR model, it assumes all nodes may be unstable, applying the  $K$ -means algorithm on all nodes.  
 356 It then selects the node closest to each cluster center as the initial node for AR-based decoding.  
 357

358 **5 EXPERIMENT**

359 Our decomposition-based FSTA and L2Seg excel on large-scale problems. In this section, we first  
 360 evaluate how L2Seg-AR, L2Seg-NAR, and L2Seg-SYN accelerate various learning and non-learning  
 361 iterative solvers on large-capacity CVRPs with long subtours. Next, we compare L2Seg against  
 362 state-of-the-art baselines on standard benchmark CVRP and VRPTW instances. Finally, we provide  
 363 in-depth analyses of our pipeline. Additional results on CVRPLib benchmarks, clustered CVRP,  
 364 heterogeneous-demand CVRP, a case study, and further discussions are presented in Appendix E.  
 365

366 **Backbone Solvers.** We apply L2Seg to three representative backbones: LKH-3 (Helsgaun, 2017)  
 367 (*classic heuristic*), LNS (Shaw, 1998) (*decomposition framework*), and L2D (Li et al., 2021) (*learning-  
 368 guided hybrid solvers, or machine-learning enhanced LNS*) to demonstrate the broad applicability.  
 369 See Appendix D.1 for details.

370 **Baselines.** We include state-of-the-art classic solvers (LKH-3 (Helsgaun, 2017), HGS (Vidal, 2022)),  
 371 neural solvers (BQ (Drakulic et al., 2023), LEHD (Luo et al., 2023), ELG (Gao et al., 2024), ICAM  
 372 (Zhou et al., 2024), L2R (Zhou et al., 2025a), SIL (Luo et al., 2024)), and learning-based divide-and-  
 373 conquer methods (GLOP (Ye et al., 2024), TAM (Hou et al., 2023), UDC (Zheng et al., 2024), L2D  
 374 (Li et al., 2021), NDS (Hottung et al., 2025)). We rerun LKH-3, LNS, L2D, and NDS and report  
 375 results from Luo et al. (2024); Zheng et al. (2024) for other baselines using the same benchmarks.  
 376 See Appendix D.2 for baseline setup details and Appendix D.3 for L2Seg hyperparameters.  
 377

378 **Data Distribution.** We generate all training and test instances following prior works Zheng et al.  
 379 (2024) for CVRP and Solomon (1987) for VRPTW. See Appendix D.4 for details. For Section 5.1,  
 380 results are averaged over 100 large-scale CVRP test instances at 2k and 5k scales (capacities 500

378  
 379  
 380  
 381  
 382  
 383  
 384  
 385  
 Table 1: Performance comparisons of our proposed L2Seg-NAR, L2Seg-AR, and L2Seg-SYN when accelerating three backbone solvers, LKH-3, LNS, and L2D, on the *large-capacity* CVRP instances. We report the objective value, improvement gain (%), and the time. The gains (the higher the better) are w.r.t. the performance of each backbone solver. Time limits were set to be 150s for CVRP2k and 240s for CVRP5k, respectively.

| Methods                | CVRP2k            |                 |                   | CVRP5k            |                 |                   |
|------------------------|-------------------|-----------------|-------------------|-------------------|-----------------|-------------------|
|                        | Obj. $\downarrow$ | Gain $\uparrow$ | Time $\downarrow$ | Obj. $\downarrow$ | Gain $\uparrow$ | Time $\downarrow$ |
| LKH-3 (Helsgaun, 2017) | 45.24             | 0.00%           | 152s              | 65.34             | 0.00%           | 242s              |
| L2Seg-NAR-LKH-3        | 44.34             | 1.99%           | 158s              | 64.72             | 0.95%           | 246s              |
| L2Seg-AR-LKH-3         | 44.23             | 2.23%           | 151s              | 64.67             | 1.03%           | 244s              |
| <b>L2Seg-SYN-LKH-3</b> | <b>43.92</b>      | <b>2.92%</b>    | 152s              | <b>64.12</b>      | <b>1.87%</b>    | 248s              |
| LNS (Shaw, 1998)       | 44.92             | 0.00%           | 154s              | 64.69             | 0.00%           | 246s              |
| L2Seg-NAR-LNS          | 44.12             | 1.78%           | 154s              | 64.38             | 0.48%           | 244s              |
| L2Seg-AR-LNS           | 44.02             | 2.00%           | 157s              | 64.24             | 0.70%           | 249s              |
| <b>L2Seg-SYN-LNS</b>   | <b>43.42</b>      | <b>3.34%</b>    | 152s              | <b>63.94</b>      | <b>1.16%</b>    | 241s              |
| L2D (Li et al., 2021)  | 43.69             | 0.00%           | 153s              | 64.21             | 0.00%           | 243s              |
| L2Seg-NAR-L2D          | 43.55             | 0.32%           | 152s              | 64.02             | 0.30%           | 243s              |
| L2Seg-AR-L2D           | 43.53             | 0.37%           | 156s              | 64.12             | 0.14%           | 247s              |
| <b>L2Seg-SYN-L2D</b>   | <b>43.35</b>      | <b>0.78%</b>    | 157s              | <b>63.89</b>      | <b>0.50%</b>    | 248s              |

398 and 1,000, respectively). For Section 5.2, we follow standard NCO benchmarks, reporting averaged  
 399 results on 1k, 2k, and 5k test datasets with 1,000 CVRP and 100 VRPTW instances per scale.

400 **Evaluation and Metric.** We impose time limits of 150s, 240s, and 300s for CVRP1k, 2k, and 5k,  
 401 and 120s, 240s, and 600s for VRPTW1k, 2k and 5k, where each solver may finish a few seconds  
 402 ( $< 10$ s) beyond its limit. We set  $\eta = 0.6$  and  $n_{\text{KMEANS}} = 3$  for our L2Seg. We report averaged  
 403 cost and per-instance solve time for all cases, and report percentage improvements over backbone in  
 404 Section 5.1 and gaps to HGS (the best heuristic solvers) for both CVRP and VRPTW in Section 5.2.  
 405

### 406 5.1 L2SEG ACCELERATES VARIOUS ITERATIVE BACKBONE SOLVERS

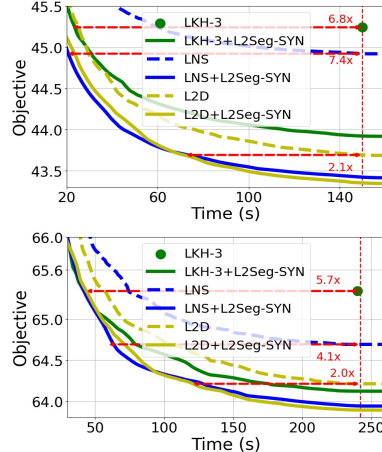
407 We first verify the effectiveness of the three L2Seg variants to enhance backbone solvers. Table 1  
 408 presents results on large-capacity, uniformly distributed CVRPs with long subtours. All L2Seg vari-  
 409 ants consistently improve each backbone across all problem scales. Also, performance gains are larger  
 410 for weaker backbones. While L2Seg-AR and L2Seg-NAR each boost performance, their combination  
 411 (L2Seg-SYN) delivers the best solutions. Figure 5 plots average objective curves over time, which re-  
 412 veal 2x to 7x speedups on the backbone solvers with L2Seg-SYN. Remarkably, L2Seg-augmentation  
 413 lets weaker solvers surpass stronger ones (e.g., LKH-3 + L2Seg-SYN outperforms vanilla LNS).  
 414

### 415 5.2 L2SEG OUTPERFORMS CLASSIC AND NEURAL BASELINES ON CVRP AND VRPTW

416 We evaluate the highest-performing L2Seg-SYN implementation with three distinct backbone solvers  
 417 and compare against state-of-the-art classical and neural approaches. As demonstrated in Table 2,  
 418 L2Seg surpasses both classical and neural baselines on CVRP and VRPTW benchmarks. For CVRP,  
 419 L2Seg achieves superior performance within comparable computational time relative to competitive  
 420 classical solvers, including HGS on larger problem instances. It also outperforms the state-of-the-art  
 421 learning-based constructive solver SIL (Luo et al., 2024) and divide-and-conquer solver L2D (Li  
 422 et al., 2021) across all problem scales. For VRPTW, L2Seg exceeds all classical and learning-based  
 423 solvers across various scales under identical time constraints, with performance advantages increasing  
 424 as problem size grows. Notably, L2Seg consistently enhances performance when integrated with any  
 425 backbone solver, demonstrating its versatility. Additional analyses are provided in Appendix E.  
 426

### 427 5.3 L2SEG PERFORMS AND GENERALIZED WELL ON MORE REALISTIC CVRP

428 To demonstrate L2Seg’s robustness beyond uniform distributions, we evaluate both in-distribution and  
 429 zero-shot generalization on instances with clustered customers and heterogeneous demands—patterns



397  
 398 Figure 5: Search curves for L2Seg on  
 399 three backbone solvers on large capacity  
 400 CVRP2k (upper) and CVRP5k (lower).  
 401 L2Seg achieves up to 7x speedups.  
 402

432 Table 2: Performance comparisons of our L2Seg-SYN-L2D against baselines on *benchmark* CVRP  
 433 and VRPTW instances. The gap % (lower the better) is w.r.t. the performance of HGS.

| 435 Methods                     | CVRP1k       |               |           | CVRP2k        |               |           | CVRP5k        |               |           |
|---------------------------------|--------------|---------------|-----------|---------------|---------------|-----------|---------------|---------------|-----------|
|                                 | 436 Obj.↓    | 436 Gap↓      | 436 Time↓ | 436 Obj.↓     | 436 Gap↓      | 436 Time↓ | 436 Obj.↓     | 436 Gap↓      | 436 Time↓ |
| HGS (Vidal, 2022)               | 41.20        | 0.00%         | 5m        | 57.20         | 0.00%         | 5m        | 126.20        | 0.00%         | 5m        |
| LKH-3 (Helsgaun, 2017)          | 42.98        | 4.32%         | 6.6m      | 57.94         | 1.29%         | 11.4m     | 175.70        | 39.22%        | 2.5m      |
| LNS (Shaw, 1998)                | 42.44        | 3.01%         | 2.5m      | 57.62         | 0.73%         | 4.0m      | 126.58        | 0.30%         | 5.0m      |
| BQ (Drakulic et al., 2023)      | 44.17        | 7.21%         | 55s       | 62.59         | 9.42%         | 3m        | 139.80        | 10.78%        | 45m       |
| LEHD (Luo et al., 2023)         | 43.96        | 6.70%         | 1.3m      | 61.58         | 7.66%         | 9.5m      | 138.20        | 9.51%         | 3h        |
| ELG (Gao et al., 2024)          | 43.58        | 5.78%         | 15.6m     | -             | -             | -         | -             | -             | -         |
| ICAM (Zhou et al., 2024)        | 43.07        | 4.54%         | 26s       | 61.34         | 7.24%         | 3.7m      | 136.90        | 8.48%         | 50m       |
| L2R (Zhou et al., 2025a)        | 44.20        | 7.28%         | 34.2s     | -             | -             | -         | 131.10        | 3.88%         | 1.8m      |
| SIL (Luo et al., 2024)          | 42.00        | 1.94%         | 1.3m      | 57.10         | -0.17%        | 2.4m      | 123.10        | -2.52%        | 5.9m      |
| TAM(LKH-3) (Hou et al., 2023)   | 46.30        | 12.38%        | 4m        | 64.80         | 13.29%        | 9.6m      | 144.60        | 14.58%        | 35m       |
| GLOP-G(LKH-3) (Ye et al., 2024) | 45.90        | 11.41%        | 2m        | 63.02         | 10.52%        | 2.5m      | 140.40        | 11.25%        | 8m        |
| UDC (Zheng et al., 2024)        | 43.00        | 4.37%         | 1.2h      | 60.01         | 4.9%          | 2.15h     | 136.70        | 8.32%         | 16m       |
| L2D (Li et al., 2021)           | 42.07        | 2.11%         | 2.5m      | 57.44         | 0.42%         | 4.2m      | 126.48        | 0.22%         | 5.3m      |
| NDS (Hottung et al., 2025)      | <b>41.16</b> | <b>-0.01%</b> | 2.5m      | 56.11         | -1.91%        | 4m        | -             | -             | -         |
| L2Seg-SYN-LKH-3                 | 41.42        | 0.53%         | 2.5m      | 56.37         | -1.45%        | 4.4m      | 122.34        | -3.16%        | 5.1m      |
| L2Seg-SYN-LNS                   | 41.36        | 0.39%         | 2.5m      | 56.08         | -1.96%        | 4.1m      | 121.96        | -3.48%        | 5.1m      |
| <b>L2Seg-SYN-L2D</b>            | 41.23        | 0.07%         | 2.5m      | <b>56.05</b>  | <b>-2.01%</b> | 4.1m      | <b>121.87</b> | <b>-3.55%</b> | 5.1m      |
| 448 Methods                     | VRPTW1k      |               |           | VRPTW2k       |               |           | VRPTW5k       |               |           |
|                                 | 449 Obj.↓    | 449 Gap↓      | 449 Time↓ | 449 Obj.↓     | 449 Gap↓      | 449 Time↓ | 449 Obj.↓     | 449 Gap↓      | 449 Time↓ |
| HGS (Vidal, 2022)               | 90.35        | 0.00%         | 2m        | 173.46        | 0.00%         | 4m        | 344.2         | 0.00%         | 10m       |
| LKH-3 (Helsgaun, 2017)          | 91.32        | 1.07%         | 2m        | 174.25        | 0.46%         | 4m        | 353.2         | 2.61%         | 10m       |
| LNS (Shaw, 1998)                | 88.12        | -2.47%        | 2m        | 165.42        | -4.64%        | 4m        | 338.5         | -1.66%        | 10m       |
| L2D (Li et al., 2021)           | 88.01        | -2.59%        | 2m        | 164.12        | -5.38%        | 4m        | 335.2         | -2.61%        | 10m       |
| NDS (Hottung et al., 2025)      | 87.54        | -3.11%        | 2m        | 167.48        | -3.45%        | 4m        | -             | -             | -         |
| L2Seg-SYN-LKH-3                 | 88.65        | -1.88%        | 2m        | 169.24        | -2.43%        | 4m        | 345.2         | 0.29%         | 10m       |
| L2Seg-SYN-LNS                   | 87.31        | -3.36%        | 2m        | 163.94        | -5.49%        | 4m        | 334.1         | -2.93%        | 10m       |
| <b>L2Seg-SYN-L2D</b>            | <b>87.25</b> | <b>-3.43%</b> | 2m        | <b>163.74</b> | <b>-5.60%</b> | 4m        | <b>333.4</b>  | <b>-3.14%</b> | 10m       |

456 Table 3: Performance of L2Seg-SYN v.s. Random FSTA to accelerate LNS on CVRP instances.

| 458 Methods | 458 LNS (Backbone) | 458 Random FSTA (40%) | 458 Random FSTA (60%) | 458 L2Seg-SYN w/o Enhanced Features | 458 L2Seg-SYN |
|-------------|--------------------|-----------------------|-----------------------|-------------------------------------|---------------|
| CVRP2k      | 44.92              | 46.24                 | 46.89                 | 43.65                               | <b>43.42</b>  |
| CVRP5k      | 64.69              | 66.72                 | 65.92                 | 64.22                               | <b>63.94</b>  |

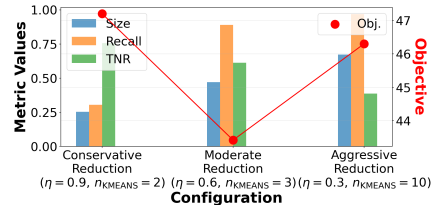
463 common in real-world logistics. As shown in Table 12, L2Seg maintains strong performance across  
 464 all settings: zero-shot transfer achieves 0.82%-3.10% improvements over LNS, while in-distribution  
 465 models reach 1.02%-3.54% gains. These consistent improvements across diverse distributions  
 466 validate L2Seg’s practical applicability. See Appendix E.3 for details.

#### 467 5.4 FURTHER ANALYSIS AND DISCUSSIONS

469 **Ablation Study.** Table 3 compares the LNS backbone; random FSTA with 40% and 60% of edges  
 470 arbitrarily marked as unstable; L2Seg-SYN w/o enhanced features; and full L2Seg-SYN. Results  
 471 show that Random FSTA worsens performance; and only full L2Seg-SYN with enhanced features  
 472 achieves top performance. This confirms that L2Seg’s learnable, feature-guided segmentation is  
 473 indispensable for preserving high-quality segments in FSTA for boosting backbone solvers.

474 **High Recall or High TNR?** Higher Recall allows more  
 475 unstable edges to be reoptimized, potentially improving  
 476 performance, while higher TNR reduces problem size and  
 477 runtime. However, due to learning imprecision, pursuing  
 478 high TNRs often reduces Recall, causing premature  
 479 convergence. Figure 7 shows that for L2Seg-SYN, fixing too  
 480 few (left: high Recall, low TNR) or too many (right: high  
 481 TNR, low Recall) degrades performance. Ours (middle)  
 482 balances this tradeoff for optimal performance.

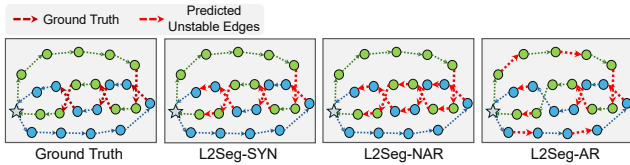
483 **Why NAR+AR Is the Best?** Figure 6 shows a conceptual  
 484 illustration of the model’s behaviour across L2Seg variants  
 485 (See Appendix E.5 for a real case-study). L2Seg-NAR identifies  
 unstable regions but over-classifies dependencies but struggles with



486 Figure 7: Statistic values of Size (reduced/original ratio), Recall, and TNR  
 487 across three L2Seg-SYN configurations.

486  
487 Table 4: Model prediction analysis of  
488 L2Seg-LNS on CVRP2k.489  
490  
491  
492

| Methods   | Recall↑       | TNR↑          | Obj.↓        |
|-----------|---------------|---------------|--------------|
| L2Seg-SYN | 89.02%        | <b>61.24%</b> | <b>43.42</b> |
| L2Seg-NAR | <b>91.46%</b> | 51.79%        | 44.02        |
| L2Seg-AR  | 74.39%        | 54.07%        | 44.12        |



517 Figure 6: Illustration of L2Seg model behaviors.

initial detection. L2Seg-SYN achieves the complementary synergy. Moreover, Table 4 further shows that L2Seg-SYN achieves the best balanced Recall and TNR for the best performance.

**The Structure of the Stability Labels.** We hypothesize that stability labels are composed of two factors: (1) Inherent Problem Structure (e.g., edges common to the majority of local optima regardless of the solver), and (2) Solver-Dependent Patterns (edges preferred due to specific search biases). We designed an experiment on CVRP1k to compare label similarity across different solvers. We generated labels using HGS (60s time limit) and LKH-3 (1000 local search steps), comparing them against a "ground truth" generated by LKH-3 with a much longer run (3000 steps). Each solver was run with 10 different seeds to remove randomness. Label similarity is defined as the percentage of overlapping stable edges. As shown in Table 5, these results reveal two key insights: (1) Even fundamentally different solvers (HGS vs. LKH-3) share 78.3% of stable edges. This indicates that the majority of the stability is contributed by inherent problem structure rather than solver artifacts; (2) More similar solvers produce more similar labels (LKH-3 variants: 85.1% similarity) compared to fundamentally different solvers (HGS vs LKH-3: 78.3%), suggesting some solver-specific patterns.

518 Table 5: Label similarity across different solvers

519  
520  
521  
522  
523  
524  
525  
526  
527  
528  
529  
530  
531  
532  
533  
534  
535  
536  
537  
538  
539

|                  | HGS   | LKH-3 (1000 Local Search Step) | LKH-3 (3000 Local Search Step) |
|------------------|-------|--------------------------------|--------------------------------|
| Label Similarity | 78.3% | 85.1%                          | 100% (by default)              |

## 6 CONCLUSION

This work introduces Learning-to-Segment (L2Seg), a novel learning-guided framework that accelerates state-of-the-art iterative solvers for large-scale VRPs by 2x to 7x. We formalize the FSTA decomposition and employ a specialized encoder-decoder architecture to dynamically differentiate potentially unstable and stable segments in FSTA. L2Seg features three variants, L2Seg-NAR, L2Seg-AR, and L2Seg-SYN, pioneering the synergy of AR and NAR models in NCO. Extensive results demonstrate L2Seg’s state-of-the-art performance on representative CVRP and VRPTW and flexibility in boosting classic and learning-based solvers, including other decomposition frameworks. One potential limitation is that L2Seg is not guaranteed to boost all VRP solvers across all VRP variants. Future work includes: (1) extending L2Seg to accelerate additional VRP solvers (e.g., Vidal (2022)); (2) applying L2Seg to more VRP variants and other combinatorial optimization problems; and (3) expanding the synergy between AR and NAR models to the broader NCO community.

## REPRODUCIBILITY STATEMENT

We provide comprehensive technical details in the appendices: architecture and input features (Appendix D.3), data generation (Appendix D.4), training procedures (Appendix C.4), and experimental setup (Section 5). The complete codebase, including code and pre-trained models, will be released on GitHub under the MIT License upon publication.

## REFERENCES

Gilbert Laporte. Fifty years of vehicle routing. *Transportation science*, 43(4):408–416, 2009.

Wouter Kool, Herke van Hoof, and Max Welling. Attention, learn to solve routing problems! In *International Conference on Learning Representations*, 2018.

540     Yoshua Bengio, Andrea Lodi, and Antoine Prouvost. Machine learning for combinatorial optimization:  
 541        a methodological tour d'horizon. *European Journal of Operational Research*, 290(2):405–421,  
 542        2021.

543     Fu Luo, Xi Lin, Zhenkun Wang, Xialiang Tong, Mingxuan Yuan, and Qingfu Zhang. Self-improved  
 544        learning for scalable neural combinatorial optimization. *arXiv preprint arXiv:2403.19561*, 2024.

545     Federico Berto, Chuanbo Hua, Junyoung Park, Laurin Luttmann, Yining Ma, Fanchen Bu, Jiarui  
 546        Wang, Haoran Ye, Minsu Kim, Sanghyeok Choi, Nayeli Gast Zepeda, André Hottung, Jianan  
 547        Zhou, Jieyi Bi, Yu Hu, Fei Liu, Hyeonah Kim, Jiwoo Son, Haeyeon Kim, Davide Angioni, Wouter  
 548        Kool, Zhiguang Cao, Jie Zhang, Kijung Shin, Cathy Wu, Sungsoo Ahn, Guojie Song, Changhyun  
 549        Kwon, Lin Xie, and Jinkyoo Park. RL4CO: an extensive reinforcement learning for combinatorial  
 550        optimization benchmark. *arXiv preprint arXiv:2306.17100*, 2023.

551     Keld Helsgaun. An extension of the lin-kernighan-helsgaun tsp solver for constrained traveling  
 552        salesman and vehicle routing problems. *Roskilde: Roskilde University*, 12:966–980, 2017.

553     Thibaut Vidal. Hybrid genetic search for the cvrp: Open-source implementation and swap\* neighbor-  
 554        hood. *Computers & Operations Research*, 140:105643, 2022.

555     Paul Shaw. Using constraint programming and local search methods to solve vehicle routing problems.  
 556        In *International conference on principles and practice of constraint programming*, pages 417–431.  
 557        Springer, 1998.

558     Sirui Li, Zhongxia Yan, and Cathy Wu. Learning to delegate for large-scale vehicle routing. *Advances  
 559        in Neural Information Processing Systems*, 34:26198–26211, 2021.

560     Roberto Baldacci, Aristide Mingozzi, and Roberto Roberti. Recent exact algorithms for solving  
 561        the vehicle routing problem under capacity and time window constraints. *European Journal of  
 562        Operational Research*, 218(1):1–6, 2012.

563     Yeong-Dae Kwon, Jinho Choo, Byoungjip Kim, Iljoo Yoon, Youngjune Gwon, and Seungjai Min.  
 564        POMO: Policy optimization with multiple optima for reinforcement learning. In *Advances in  
 565        Neural Information Processing Systems*, volume 33, pages 21188–21198, 2020.

566     Han Fang, Zhihao Song, Paul Weng, and Yutong Ban. Invit: A generalizable routing problem  
 567        solver with invariant nested view transformer. In *Forty-first International Conference on Machine  
 568        Learning*, 2024.

569     Simon Geisler, Johanna Sommer, Jan Schuchardt, Aleksandar Bojchevski, and Stephan Günnemann.  
 570        Generalization of neural combinatorial solvers through the lens of adversarial robustness. In  
 571        *International Conference on Learning Representations*, 2022.

572     Chengrui Gao, Haopu Shang, Ke Xue, Dong Li, and Chao Qian. Towards generalizable neural solvers  
 573        for vehicle routing problems via ensemble with transferrable local policy. In *Proceedings of the  
 574        Thirty-First International Joint Conference on Artificial Intelligence*, 2024.

575     Darko Drakulic, Sofia Michel, Florian Mai, Arnaud Sors, and Jean-Marc Andreoli. BQ-NCO:  
 576        Bisimulation quotienting for generalizable neural combinatorial optimization. In *Advances in  
 577        Neural Information Processing Systems*, 2023.

578     Chaoyang Wang, Pengzhi Cheng, Jingze Li, and Weiwei Sun. Leader reward for pomo-based neural  
 579        combinatorial optimization. *arXiv preprint arXiv:2405.13947*, 2024.

580     Yimeng Min, Yiwei Bai, and Carla P Gomes. Unsupervised learning for solving the travelling  
 581        salesman problem. *Advances in Neural Information Processing Systems*, 2023.

582     Yang Li, Jinpei Guo, Runzhong Wang, and Junchi Yan. From distribution learning in training  
 583        to gradient search in testing for combinatorial optimization. *Advances in Neural Information  
 584        Processing Systems*, 2023a.

585     Han Lu, Zenan Li, Runzhong Wang, Qibing Ren, Xijun Li, Mingxuan Yuan, Jia Zeng, Xiaokang  
 586        Yang, and Junchi Yan. ROCO: A general framework for evaluating robustness of combinatorial  
 587        optimization solvers on graphs. In *International Conference on Learning Representations*, 2023.

594 Taoan Huang, Aaron M Ferber, Arman Zharmagambetov, Yuandong Tian, and Bistra Dilkina.  
 595 Contrastive predict-and-search for mixed integer linear programs. In Ruslan Salakhutdinov, Zico  
 596 Kolter, Katherine Heller, Adrian Weller, Nuria Oliver, Jonathan Scarlett, and Felix Berkenkamp,  
 597 editors, *Proceedings of the 41st International Conference on Machine Learning*, volume 235 of  
 598 *Proceedings of Machine Learning Research*, pages 19757–19771. PMLR, 21–27 Jul 2024. URL  
 599 <https://proceedings.mlr.press/v235/huang24f.html>.

600 Taoan Huang, Aaron M Ferber, Yuandong Tian, Bistra Dilkina, and Benoit Steiner. Searching large  
 601 neighborhoods for integer linear programs with contrastive learning. In *International Conference  
 602 on Machine Learning*, pages 13869–13890. PMLR, 2023.

603 André Hottung, Paula Wong-Chung, and Kevin Tierney. Neural deconstruction search for vehicle  
 604 routing problems. *Transactions on Machine Learning Research*, 2025.

605 Fu Luo, Xi Lin, Fei Liu, Qingfu Zhang, and Zhenkun Wang. Neural combinatorial optimization with  
 606 heavy decoder: Toward large scale generalization. *Advances in Neural Information Processing  
 607 Systems*, 36:8845–8864, 2023.

608 Zhi Zheng, Changliang Zhou, Tong Xialiang, Mingxuan Yuan, and Zhenkun Wang. Udc: A unified  
 609 neural divide-and-conquer framework for large-scale combinatorial optimization problems. In  
 610 *Advances in Neural Information Processing Systems*, 2024.

611 Yining Ma, Jingwen Li, Zhiguang Cao, Wen Song, Le Zhang, Zhenghua Chen, and Jing Tang.  
 612 Learning to iteratively solve routing problems with dual-aspect collaborative transformer. In  
 613 *Advances in Neural Information Processing Systems*, volume 34, pages 11096–11107, 2021.

614 Yining Ma, Zhiguang Cao, and Yeow Meng Chee. Learning to search feasible and infeasible regions  
 615 of routing problems with flexible neural k-opt. In *Advances in Neural Information Processing  
 616 Systems*, volume 36, 2023.

617 Minjun Kim, Junyoung Park, and Jinkyoo Park. Learning to cross exchange to solve min-max vehicle  
 618 routing problems. In *The Eleventh International Conference on Learning Representations*, 2023.

619 André Hottung and Kevin Tierney. Neural large neighborhood search for routing problems. *Artificial  
 620 Intelligence*, page 103786, 2022.

621 Yining Ma, Jingwen Li, Zhiguang Cao, Wen Song, Hongliang Guo, Yuejiao Gong, and Yeow Meng  
 622 Chee. Efficient neural neighborhood search for pickup and delivery problems. In *Proceedings of the  
 623 Thirty-First International Joint Conference on Artificial Intelligence, IJCAI-22*, pages 4776–4784,  
 624 7 2022.

625 André Hottung, Yeong-Dae Kwon, and Kevin Tierney. Efficient active search for combinatorial  
 626 optimization problems. In *International Conference on Learning Representations*, 2022.

627 Minsu Kim, Jinkyoo Park, and joungho kim. Learning collaborative policies to solve np-hard routing  
 628 problems. In *Advances in Neural Information Processing Systems*, volume 34, pages 10418–10430,  
 629 2021.

630 Zhiqing Sun and Yiming Yang. Difusco: Graph-based diffusion solvers for combinatorial optimization.  
 631 In *Advances in Neural Information Processing Systems*, 2023.

632 Felix Chalumeau, Shikha Surana, Clément Bonnet, Nathan Grinsztajn, Arnu Pretorius, Alexandre  
 633 Laterre, and Thomas D Barrett. Combinatorial optimization with policy adaptation using latent  
 634 space search. In *Advances in Neural Information Processing Systems*, 2023.

635 Minsu Kim, Sanghyeok Choi, Jiwoo Son, Hyeonah Kim, Jinkyoo Park, and Yoshua Bengio. Ant  
 636 colony sampling with glownets for combinatorial optimization. *arXiv preprint arXiv:2403.07041*,  
 637 2024.

638 Ruizhong Qiu, Zhiqing Sun, and Yiming Yang. Dimes: A differentiable meta solver for combinatorial  
 639 optimization problems. *Advances in Neural Information Processing Systems*, 35:25531–25546,  
 640 2022.

648 Alberto Santini, Michael Schneider, Thibaut Vidal, and Daniele Vigo. Decomposition strategies for  
 649 vehicle routing heuristics. *INFORMS Journal on Computing*, 35(3):543–559, 2023.  
 650

651 Zefang Zong, Hansen Wang, Jingwei Wang, Meng Zheng, and Yong Li. Rbg: Hierarchically solving  
 652 large-scale routing problems in logistic systems via reinforcement learning. In *Proceedings of the*  
 653 *28th ACM SIGKDD Conference on Knowledge Discovery and Data Mining*, pages 4648–4658,  
 654 2022.

655 Qingchun Hou, Jingwei Yang, Yiqiang Su, Xiaoqing Wang, and Yuming Deng. Generalize learned  
 656 heuristics to solve large-scale vehicle routing problems in real-time. In *The Eleventh International*  
 657 *Conference on Learning Representations*, 2023.

658 Changliang Zhou, Xi Lin, Zhenkun Wang, and Qingfu Zhang. L2r: Learning to reduce search space  
 659 for generalizable neural routing solver. *arXiv preprint arXiv:2503.03137*, 2025a.  
 660

661 Shipei Zhou, Yuandong Ding, Chi Zhang, Zhiguang Cao, and Yan Jin. Dualopt: A dual  
 662 divide-and-optimize algorithm for the large-scale traveling salesman problem. *arXiv preprint*  
 663 *arXiv:2501.08565*, 2025b.

664 Yuxin Pan, Ruohong Liu, Yize Chen, Zhiguang Cao, and Fangzhen Lin. Hierarchical learning-based  
 665 graph partition for large-scale vehicle routing problems. *arXiv preprint arXiv:2502.08340*, 2025.  
 666

667 Ke Li, Fei Liu, Zhenkun Wang, and Qingfu Zhang. Destroy and repair using hyper-graphs for routing.  
 668 In *Proceedings of the AAAI Conference on Artificial Intelligence*, volume 39, pages 18341–18349,  
 669 2025.

670 Zhang-Hua Fu, Sipeng Sun, Jintong Ren, Tianshu Yu, Haoyu Zhang, Yuanyuan Liu, Lingxiao Huang,  
 671 Xiang Yan, and Pinyan Lu. A hierarchical destroy and repair approach for solving very large-scale  
 672 travelling salesman problem. *arXiv preprint arXiv:2308.04639*, 2023.  
 673

674 Mouad Morabit, Guy Desaulniers, and Andrea Lodi. Learning to repeatedly solve routing problems.  
 675 *Networks*, 83(3):503–526, 2024.

676 Yang Li, Jinpei Guo, Runzhong Wang, and Junchi Yan. T2t: From distribution learning in training  
 677 to gradient search in testing for combinatorial optimization. In *Advances in Neural Information*  
 678 *Processing Systems*, 2023b.  
 679

680 Haoran Ye, Jiarui Wang, Helan Liang, Zhiguang Cao, Yong Li, and Fanzhang Li. Glop: Learning  
 681 global partition and local construction for solving large-scale routing problems in real-time. In  
 682 *Proceedings of the AAAI Conference on Artificial Intelligence*, 2024.

683 A Vaswani. Attention is all you need. *Advances in Neural Information Processing Systems*, 2017.  
 684

685 Petar Veličković, Guillem Cucurull, Arantxa Casanova, Adriana Romero, Pietro Lio, and Yoshua  
 686 Bengio. Graph attention networks. *arXiv preprint arXiv:1710.10903*, 2017.

687 Birger Funke, Tore Grünert, and Stefan Irnich. Local search for vehicle routing and scheduling  
 688 problems: Review and conceptual integration. *Journal of heuristics*, 11:267–306, 2005.  
 689

690 Junyoung Chung, Caglar Gulcehre, KyungHyun Cho, and Yoshua Bengio. Empirical evaluation of  
 691 gated recurrent neural networks on sequence modeling. *arXiv preprint arXiv:1412.3555*, 2014.

692 Changliang Zhou, Xi Lin, Zhenkun Wang, Xialiang Tong, Mingxuan Yuan, and Qingfu Zhang.  
 693 Instance-conditioned adaptation for large-scale generalization of neural combinatorial optimization.  
 694 *arXiv preprint arXiv:2405.01906*, 2024.  
 695

696 Marius M Solomon. Algorithms for the vehicle routing and scheduling problems with time window  
 697 constraints. *Operations research*, 35(2):254–265, 1987.

698 Marc Goetschalckx and Charlotte Jacobs-Blecha. The vehicle routing problem with backhauls.  
 699 *European Journal of Operational Research*, 42(1):39–51, 1989.  
 700

701 Goran Martinovic, Ivan Aleksi, and Alfonzo Baumgartner. Single-commodity vehicle routing problem  
 with pickup and delivery service. *Mathematical Problems in Engineering*, 2008(1):697981, 2008.

702 Eduardo Uchoa, Diego Pecin, Artur Pessoa, Marcus Poggi, Thibaut Vidal, and Anand Subramanian.  
703 New benchmark instances for the capacitated vehicle routing problem. *European Journal of  
704 Operational Research*, 257(3):845–858, 2017.  
705  
706 Florian Arnold, Michel Gendreau, and Kenneth Sørensen. Efficiently solving very large-scale routing  
707 problems. *Computers & operations research*, 107:32–42, 2019.  
708  
709  
710  
711  
712  
713  
714  
715  
716  
717  
718  
719  
720  
721  
722  
723  
724  
725  
726  
727  
728  
729  
730  
731  
732  
733  
734  
735  
736  
737  
738  
739  
740  
741  
742  
743  
744  
745  
746  
747  
748  
749  
750  
751  
752  
753  
754  
755

|     |   |           |
|-----|---|-----------|
| 756 | APPENDICES  |           |
| 757 |   |           |
| 758 |   |           |
| 759 | CONTENTS  |           |
| 760 |   |           |
| 761 | <b>A Supplementary Definitions</b>  | <b>16</b> |
| 762 |   |           |
| 763 | A.1 Unstable Edges and Stable Edges . . . . .                                 | 16        |
| 764 | A.2 Capacitated Vehicle Routing Problem . . . . .                             | 16        |
| 765 | A.3 Vehicle Routing Problem with Time Windows . . . . .                       | 16        |
| 766 |   |           |
| 767 |   |           |
| 768 | <b>B Details of First-Segment-Then-Aggregate (FSTA)</b>                       | <b>16</b> |
| 769 |   |           |
| 770 | B.1 More discussions on FSTA . . . . .  | 16        |
| 771 | B.2 Proof of FSTA . . . . .   | 21        |
| 772 |   |           |
| 773 |   |           |
| 774 | <b>C L2Seg Details</b>  | <b>26</b> |
| 775 |   |           |
| 776 | C.1 Comparative Analysis of L2Seg Against Existing Methods . . . . .          | 26        |
| 777 | C.2 Input Feature Design Details . . . . .                                    | 27        |
| 778 | C.3 Masking Details . . . . .   | 27        |
| 779 | C.4 Training Data Collection Details . . . . .                                | 28        |
| 780 | C.5 Inference Details . . . . .   | 28        |
| 781 |   |           |
| 782 |   |           |
| 783 |   |           |
| 784 | <b>D Experimental and Implementation Details</b>                              | <b>28</b> |
| 785 |   |           |
| 786 | D.1 Backbone solvers . . . . .  | 28        |
| 787 | D.2 Baselines . . . . .   | 31        |
| 788 | D.3 Parameters and Training Hyperparameters . . . . .                         | 31        |
| 789 | D.4 Instance Generation . . . . .   | 32        |
| 790 |   |           |
| 791 |   |           |
| 792 | <b>E Additional Experiments and Analysis</b>                                  | <b>33</b> |
| 793 |   |           |
| 794 | E.1 Hyperparameter Study . . . . .  | 33        |
| 795 | E.2 Results on Realistic Routing Datasets . . . . .                           | 33        |
| 796 | E.3 Results on Clustered CVRP and Heterogeneous-demand CVRP . . . . .         | 34        |
| 797 | E.4 Standard Deviation Comparison . . . . .                                   | 34        |
| 798 | E.5 Case Study: Comparison of Predictions of Three L2Seg Approaches . . . . . | 35        |
| 799 | E.6 Unstable and Stable Edges Convergence . . . . .                           | 35        |
| 800 | E.7 The Neural Network Overheads of L2Seg . . . . .                           | 36        |
| 801 | E.8 Time of Training L2Seg . . . . .  | 36        |
| 802 |   |           |
| 803 |   |           |
| 804 |   |           |
| 805 |   |           |
| 806 |   |           |
| 807 | <b>F Broader Impacts</b>  | <b>36</b> |
| 808 |   |           |
| 809 | <b>G Large Language Models Usage</b>  | <b>37</b> |

810 A SUPPLEMENTARY DEFINITIONS  
811812 A.1 UNSTABLE EDGES AND STABLE EDGES  
813814 We define an **iterative step**  $t$  as the  $t$ -th invocation of the backbone solver. Within each invocation,  
815 the solver performs a full round of optimization (involving multiple local search operations) subject  
816 to a fixed budget (e.g., time limit or number of steps) to return a locally optimal solution. Unstable  
817 edges refer to edges that need to be re-optimized during the iterative re-optimization procedure. We  
818 supplement the formal definitions as follows: given a solution  $\mathcal{R}_t$  at iterative step  $t$ , an edge  $e \in \mathcal{R}$  is  
819 unstable if  $e \notin \mathcal{R}_{t+1}$ . When we generate the labels for training, we use a lookahead backbone solver  
820 for detecting unstable edges. An edge is a stable edge if it's not an unstable edge.  
821822 A.2 CAPACITATED VEHICLE ROUTING PROBLEM  
823824 Given a complete graph  $G = (V, E)$  where  $V = \{x_0, x_1, \dots, x_n\}$  is the set of nodes with node  $x_0$   
825 representing the depot and nodes  $x_1$  to  $x_n$  representing customers. Each customer  $i$  has a demand  
826  $d_i > 0$ , and each edge  $e_{i,j} \in E$  has an associated cost representing the travel distance or travel time  
827 between nodes  $x_i$  and  $x_j$ . A fleet of homogeneous vehicles, each with capacity  $C$ , is available at the  
828 depot. The objective is to find a set of routes that minimizes the total travel cost, subject to: (i) each  
829 route starts and ends at the depot, (ii) each customer is visited exactly once, (iii) the total demand of  
830 customers on each route does not exceed vehicle capacity  $C$ .  
831832 A.3 VEHICLE ROUTING PROBLEM WITH TIME WINDOWS  
833834 Given a complete graph  $G = (V, E)$  where  $V = \{x_0, x_1, \dots, x_n\}$  is the set of nodes with node  $x_0$   
835 representing the depot and nodes  $x_1$  to  $x_n$  representing customers. Each customer  $i$  has a demand  
836  $d_i > 0$ , and each edge  $e_{i,j} \in E$  has an associated cost representing the travel distance or travel time  
837 between nodes  $x_i$  and  $x_j$ . Each customer  $i$  has a time window  $[t_i^l, t_i^r]$  where  $t_i^l$  is the earliest arrival  
838 time and  $t_i^r$  is the latest arrival time, and requires a service time  $s_i$ . A fleet of homogeneous vehicles,  
839 each with capacity  $C$ , is available at the depot. The objective is to find a set of routes that minimizes  
840 the total travel cost, subject to: (i) each route starts and ends at the depot, (ii) each customer is visited  
841 exactly once, (iii) the total demand of customers on each route does not exceed vehicle capacity  $C$ ,  
842 (iv) service at each customer begins within their time window  $[t_i^l, t_i^r]$ .  
843844 B DETAILS OF FIRST-SEGMENT-THEN-AGGREGATE (FSTA)  
845846 B.1 MORE DISCUSSIONS ON FSTA  
847848 B.1.1 VISUALIZATION OF UNSTABLE EDGE PATTERNS  
849850 In this section, we provide visualization and analysis of unstable edge distribution patterns, which  
851 serve as foundational motivation for our L2Seg approach. We examine unstable edges on three  
852 randomly selected CVRP1k instances solved iteratively using LKH-3. In these visualizations, red  
853 dashed lines represent unstable edges, and yellow stars indicate depot locations.  
854855 Our visualization reveals two key observations: (1) The number of unstable edges generally decreases  
856 as optimization progresses, with more and more edges remaining unchanged between iterations; (2)  
857 Edges at route boundaries exhibit higher stability, while unstable edges predominantly concentrate  
858 within route interiors. Despite these discernible spatial patterns, no simple heuristic rule appears  
859 sufficient to reliably predict unstable edges, as they can be distributed across the start, middle, and  
860 end segments of each tour. This complexity motivates our development of L2Seg, a learning-based  
861 method designed to capture these intricate patterns more effectively.  
862863 B.1.2 VISUALIZATION OF APPLYING FSTA ON ONE CVRP INSTANCE  
864865 To provide a concrete illustration of our FSTA methodology, we present an example of its application  
866 to CVRP in Figure 9, which demonstrates the complete FSTA decomposition pipeline (detailed  
867 algorithmic specifications are provided in Appendix B.1.4). This example utilizes the lookahead  
868 oracle model for unstable edge identification (defined in Appendix B.1.1), employs LKH-3 as the  
869

864 backbone optimization solver, and operates on a representative small-capacity CVRP1k instance  
 865 to showcase the framework’s efficacy. Red dashed lines indicate detected unstable edges, while  
 866 blue dashed lines represent re-optimized edges. Note that dual hypernode aggregation substantially  
 867 reduces the problem size compared to the original instance.

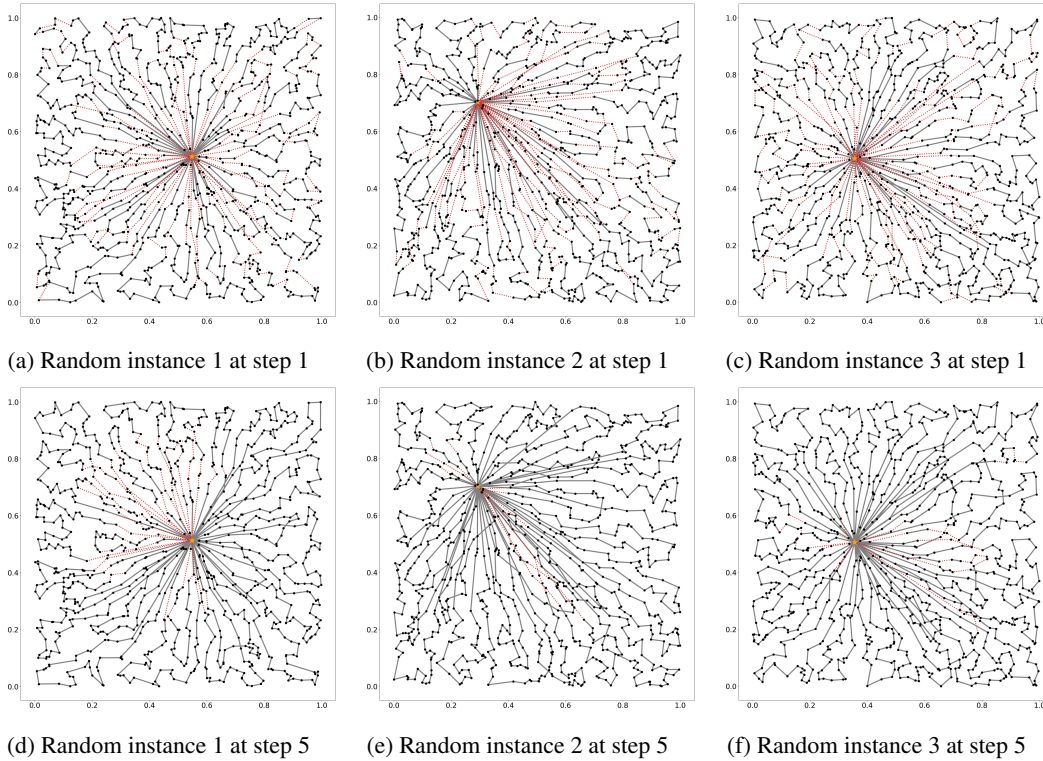
868  
 869 **B.1.3 ASSUMPTION VERIFICATION**  
 870

871 Table 6: Oracle Performance on CVRP2k: Time to Reach L2Seg-SYN-LNS Solution Quality  
 872

|      | Oracle (LNS) +<br>perfect recall<br>& TNR | Oracle (LNS) +<br>95% recall<br>& 95% TNR | Oracle (LNS) +<br>90% recall<br>& 90% TNR | Oracle +<br>70% recall<br>& 70% TNR | Ref<br>(L2Seg-SYN-LNS) |
|------|---|---|---|-------------------------------------|------------------------|
| Obj. | 56.02                                     | 56.01                                     | 56.02                                     | 56.04                               | 56.08                  |
| Time | 39s                                       | 62s                                       | 119s                                      | 324s                                | 241s                   |

873  
 874 In Section 3, we hypothesized that effective problem reduction can substantially accelerate re-  
 875 optimization. We empirically validate this by implementing a look-ahead oracle for unstable edge  
 876 detection. The oracle performs a 1-step re-optimization using LKH-3 and identifies unstable edges  
 877  $E_{\text{unstable}}$  as those differing between the original and re-optimized solutions. FSTA then constructs a  
 878 reduced problem instance based on these oracle-identified edges, which is subsequently re-optimized  
 879 using the LKH-3 backbone solver. As this is an oracle-based evaluation, the time required for  
 880 look-ahead computation is excluded from performance measurements.

881 Table 6 reports the time required to achieve performance equivalent to our learned model on small-  
 882 capacity CVRP2k instances. Beyond the perfect oracle scenario, we evaluate imperfect oracle  
 883



900 Figure 8: Spatial distribution of unstable edges (dashed red lines) across optimization iterations using  
 901 LKH-3 solver. Results are presented for three randomly selected CVRP1k instances at iteavie search  
 902 steps 1 and 5. While many edges remain unchanged across iterations, unstable edges predominantly  
 903 emerge within the interiors of routes. In contrast, edges located at route boundaries exhibit higher  
 904 stability throughout the iterative optimization process.  
 905  
 906  
 907  
 908  
 909  
 910  
 911  
 912  
 913

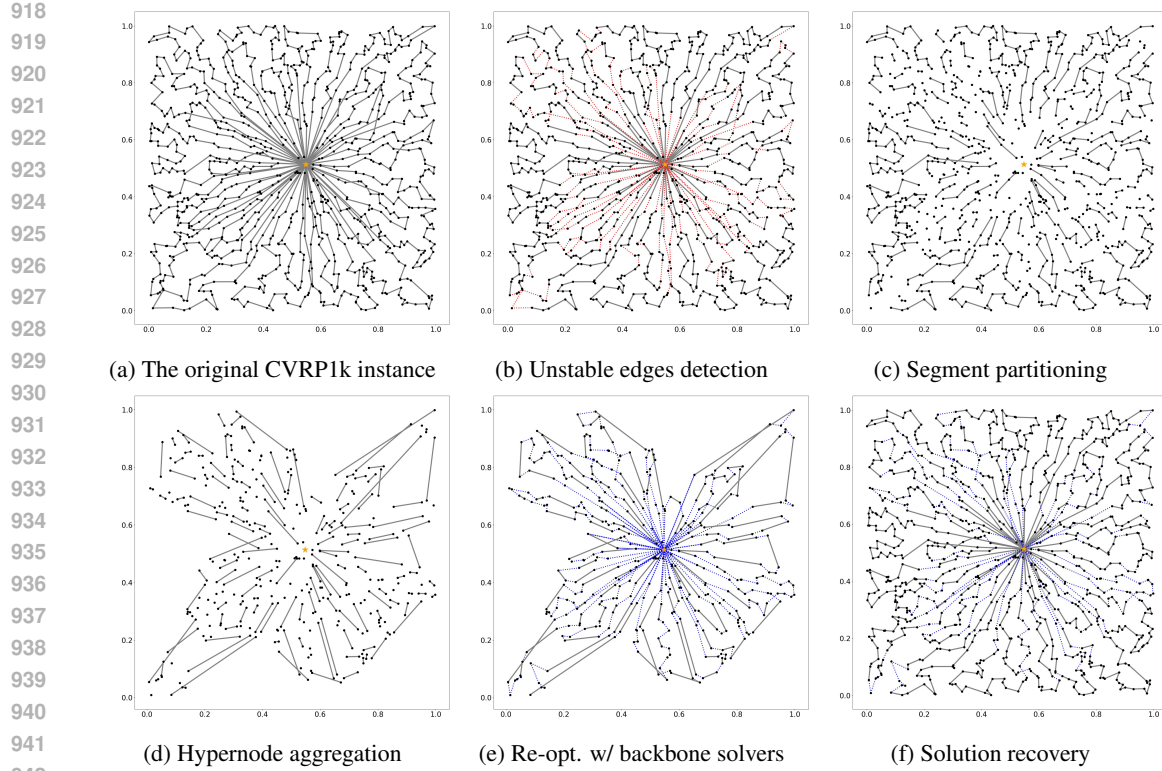


Figure 9: Illustration of our FSTA applied to one CVRP instance. Each FSTA step corresponds to the descriptions in Appendix B.1.4. Red dashed lines: unstable edges; blue dashed lines: re-optimized edges. Note that the subproblem (d) contains substantially fewer nodes than the original instance (a).

configurations where recall and true negative rates fall below 100%. The perfect oracle demonstrates substantially superior efficiency. Performance remains competitive under moderate imperfection levels; however, achieving recall and TNR as high as 90% without oracle access is highly non-trivial. In more practical scenarios, where recall and TNR drop to 70%, the oracle-based approach is outperformed by our L2Seg-SYN-LNS, highlighting the effectiveness of our learned model.

These results provide evidence that accurate identification of unstable edges, coupled with appropriate FSTA-based problem reduction, enables significantly more efficient re-optimization.

#### B.1.4 DETAILS OF FSTA DECOMPOSITION FRAMEWORK

In this section, we present the details of the FSTA decomposition framework. Given a routing problem  $P$  and an initial solution  $\mathcal{R}$ , one iterative step of FSTA yields a potentially improved solution  $\mathcal{R}_+$ . The framework comprises five sequential steps (also illustrated in Algorithm 1 and Figure 2):

1. **Unstable Edges Detection:** We implement effective methods (e.g., our learning-based model L2Seg or random heuristics detailed in Section 5.4) to identify unstable edges  $E_{\text{unstable}}$  and obtain the stable edge set  $E_{\text{stable}} = E \setminus E_{\text{unstable}}$ . This identification challenge is addressed by our L2Seg model, with full details provided in Section 4 and Appendix C.
2. **Segment Partitioning:** After removing unstable edges  $E_{\text{unstable}}$ , each route decomposes into multiple disjoint segments consisting of consecutive nodes connected by stable edges. Formally, we segment each route into  $(x_0, S_{1,j_1}^i, S_{j_1,j_2}^i, \dots, x_0) = (x_0, S_{(1)}^i, S_{(2)}^i, \dots, x_0) \in R^i$ , where  $x_0$  is depot and we simplify the notation by using a single index for segments (note that a segment can consist only one single node).
3. **Hypernode Aggregation:** We aggregate each segment  $S_{j,k}^i$  and represent it with either one hypernode ( $\tilde{S}_{j,k}^i = \{\tilde{x}_{j,k}^i\}$ ) or two hypernodes ( $\tilde{S}_{j,k}^i = \{\tilde{x}_j^i, \tilde{x}_k^i\}$ ) with aggregated attributes.

972 This transformation requires that (our feasibility theorem): (a) the reduced problem remains  
 973 feasible, and (b) a solution in the aggregated problem can be mapped back to a feasible  
 974 solution in the original problem. These transformations produce a reduced problem  $\tilde{P}$  with  
 975 corresponding solution  $\tilde{\mathcal{R}}$ .  
 976

977 **4. Re-optimization with Backbone Solvers:** We invoke a backbone solver to improve solution  
 978  $\tilde{\mathcal{R}}$ , yielding an enhanced solution  $\tilde{\mathcal{R}}_+$ . While theoretically any solver could serve as the  
 979 backbone solver, practical acceleration requires solvers capable of effectively leveraging  
 980 existing solutions (e.g., LKH-3 (Helsgaun, 2017)).  
 981

982 **5. Solution Recovery:** With the improved solution  $\tilde{\mathcal{R}}_+$  for the reduced problem  $\tilde{P}$ , we recover  
 983 a corresponding solution  $\mathcal{R}_+$  for the original problem  $P$  by expanding each hypernode back  
 984 into its original segment of nodes. This step relies on our monotonicity theorem, which  
 985 guarantees that an improved solution in  $\tilde{P}$  maps to an improved solution in  $P$ .  
 986

987 **Selection of Hypernode Aggregation Strategies.** We analyze the trade-offs between single and dual  
 988 hypernode aggregation strategies: (1) *Dual hypernode aggregation* enables bidirectional segment  
 989 traversal, potentially improving re-optimization efficiency by expanding the solution search space.  
 990 However, this approach requires enforcing inclusion of the connecting edge between hypernodes,  
 991 adding algorithmic complexity. (2) *Single hypernode aggregation* achieves superior problem size  
 992 reduction but constrains segment traversal to a fixed direction, thereby restricting the re-optimization  
 993 search space and potentially limiting performance improvements. Additionally, single hypernode  
 994 aggregation transforms symmetric routing problems into asymmetric variants, which may compromise  
 995 the efficiency of existing backbone solvers that are typically optimized for symmetric instances.  
 996

997 **Selection of Backbone Solvers.** Our framework is generic to be applied to most existing VRP  
 998 heuristics by design. In practice, acceleration within our framework requires solvers that can  
 999 effectively utilize initial solutions as warm starts. Furthermore, if the dual hypernode aggregation  
 1000 is used, the backbone solver needs to fix certain edges during local search. Our framework is  
 1001 readily compatible with a variety of solvers without modifying their source codes, including LKH-3  
 1002 (Helsgaun, 2017), decomposition-based solvers like LNS (Shaw, 1998), and learning-based methods  
 1003 such as L2D (Li et al., 2021). Incorporating additional solvers such as HGS (Vidal, 2022), would  
 1004 involve extending its current code to accept initial solutions as input, which we leave as future  
 1005 work. Notably, as demonstrated in Section 5, our L2Seg-augmented approach with relatively weaker  
 1006 backbone solvers outperforms HGS in multiple CVRP and VRPTW benchmark scenarios.  
 1007

1008 **Applicability to Routing Variants.** FSTA is broadly applicable to routing problem variants that  
 1009 support feasible hypernode aggregation and solution recovery, as ensured by the feasibility and mono-  
 1010 tonicity conditions established in Section 3. In Appendix B.2, we formally prove that many routing  
 1011 variants meet these conditions, demonstrating the versatility of our L2Seg framework. Detailed  
 1012 implementation guidelines for applying hypernode aggregation across different routing variants are  
 1013 provided in Appendix B.1.5.  
 1014

---

1012 **Algorithm 1:** Iteratively Re-optimize Routing Problems with FSTA

---

1013 **Input:** Routing problem  $P$ , initial solution  $\mathcal{R}$ , time limit  $T_{TL}$ , backbone solver BS, model M to  
 1014 identify unstable edges

1015 **Output:** Improved solution  $\mathcal{R}$

```

1016 1 while time limit  $T_{TL}$  is not reached do
1017 2    $E_{\text{unstable}} \leftarrow M(P, \mathcal{R})$ ;                                // Unstable Edges Detection
1018 3    $\{S_{j,k}^i\} \leftarrow \text{GetSegments}(P, \mathcal{R}, E_{\text{unstable}})$ ;          // Segment Partitioning
1019 4   Obtain  $\{\tilde{S}_{j,k}^i\}$  and reduced problem  $\tilde{P}$  with solution  $\tilde{\mathcal{R}}$ ; // Hypernode Aggregation
1020 5    $\tilde{\mathcal{R}}_+ \leftarrow \text{BS}(\tilde{P}, \tilde{\mathcal{R}})$ ;                                // Re-optimization with Backbone Solver
1021 6    $\mathcal{R}_+ \leftarrow \text{RecoverSolution}(P, \tilde{P}, \tilde{\mathcal{R}}_+)$ ;                  // Solution Recovery
1022 7    $\mathcal{R} \leftarrow \mathcal{R}_+$ ;                                         // Update current solution
1023 8 end while
1024 9 return  $\mathcal{R}$ 
1025

```

---

1026 B.1.5 APPLYING FSTA ON VARIOUS VRPs  
1027

1028 In this section, we present the implementation details of FSTA across diverse routing variants,  
1029 including the Capacitated Vehicle Routing Problem (CVRP), Vehicle Routing Problem with Time  
1030 Windows (VRPTW), Vehicle Routing Problem with Backhauls (VRPB), and Single-Commodity  
1031 Vehicle Routing Problem with Pickup and Delivery (1-VRPPD). Without loss of generality, we  
1032 denote a segment to be aggregated as  $S_{j,k} = (x_j \rightarrow \dots \rightarrow x_k)$ , and its corresponding hypernode  
1033 representation as either  $\tilde{S}_{j,k} = \{\tilde{x}\}$  (single hypernode) or  $\tilde{S}_{j,k} = \{\tilde{x}_j, \tilde{x}_k\}$  (dual hypernodes). The  
1034 implementation specifications are summarized in Table 7.

1035 **CVRP.** We provide the formal definition of CVRP in Section 3. Each node in CVRP is characterized  
1036 by location and demand attributes. For CVRP, we employ dual hypernode aggregation where location  
1037 attributes are preserved as  $\tilde{x}_j = x_j$  and  $\tilde{x}_k = x_k$ , while demand is equally distributed between  
1038 hypernodes as  $\tilde{d}_j = \tilde{d}_k = \frac{1}{2}(d_j + \dots + d_k)$ . We force the solver to include the edge connecting  $\tilde{x}_j$   
1039 and  $\tilde{x}_k$  in the solution.

1040 **VRPTW.** We provide the formal definition of VRPTW in Section 3. In addition to location and  
1041 demand attributes, VRPTW instances are characterized by time windows  $[t^l, t^r]$  and service time  
1042  $s$  for each node. For VRPTW, we employ adaptive strategies for hypernode aggregation based on  
1043 temporal feasibility. We first compute the aggregated time windows  $\bar{t}_j^l, \bar{t}_j^r$  and aggregated service  
1044 time  $\bar{s}_j$  using the following recursive formulation:

$$\begin{aligned} t_m^l &= \begin{cases} t_k^l & \text{if } m = k \\ \max\{t_m^l, \bar{t}_{m+1}^l - (s_m + \text{dist}(x_m, x_{m+1}))\} & \text{if } j \leq m \leq k-1, \end{cases} \\ \bar{t}_m^r &= \begin{cases} t_k^r & \text{if } m = k \\ \min\{t_m^r, \bar{t}_{m+1}^r - (s_m + \text{dist}(x_m, x_{m+1}))\} & \text{if } j \leq m \leq k-1, \end{cases} \\ \bar{s}_m &= \begin{cases} s_k & \text{if } m = k \\ \bar{s}_{m+1} + s_m + \text{dist}(x_m, x_{m+1}) & \text{if } j \leq m \leq k-1, \end{cases} \end{aligned} \quad (3)$$

1053 where  $[t_m^l, t_m^r]$  denotes the time window for node  $x_m$ ,  $s_m$  represents the service time at node  $x_m$ ,  
1054 and  $\text{dist}(x_m, x_{m+1})$  is the travel time from node  $x_m$  to node  $x_{m+1}$ .  
1055

1056 If  $\bar{t}_j^l \leq \bar{t}_j^r$  (feasible time window), we employ single hypernode aggregation with:  $\text{dist}(x_i, \tilde{x}) =$   
1057  $\text{dist}(x_i, x_j)$ ,  $\text{dist}(\tilde{x}, x_i) = \text{dist}(x_k, x_i)$ ,  $\tilde{d} = d_j + \dots + d_k$ ,  $\tilde{t}^l = \bar{t}_j^l$ ,  $\tilde{t}^r = \bar{t}_j^r$ , and  $\tilde{s} = \bar{s}_j$ .  
1058

1059 If  $\bar{t}_j^l > \bar{t}_j^r$  (temporal infeasible time window), we employ dual hypernode aggregation with:  $\tilde{x}_j = x_j$ ,  
1060  $\tilde{x}_k = x_k$ ,  $\tilde{d}_j = \tilde{d}_k = \frac{1}{2}(d_j + \dots + d_k)$ , time windows  $\tilde{t}_j^l = 0$ ,  $\tilde{t}_j^r = \bar{t}_j^r$ ,  $\tilde{t}_k^l = \bar{t}_j^l$ ,  $\tilde{t}_k^r = \infty$ , and  
1061 service times  $\tilde{s}_j = 0$ ,  $\tilde{s}_k = \bar{s}_j$ . We additionally set  $\text{dist}(\tilde{x}_j, \tilde{x}_k) = 0$  and enforce inclusion of the  
1062 edge connecting  $\tilde{x}_j$  and  $\tilde{x}_k$  in the solution.

1063 **VRPB.** Compared to the CVRP, the VRPB (Goetschalckx and Jacobs-Blecha, 1989) involves serving  
1064 two types of customers: linehaul customers requiring deliveries from the depot and backhaul cus-  
1065 tomers providing goods to be collected and returned to the depot. The primary constraint is that all  
1066 linehaul customers must be visited before any backhaul customers on the same route, while ensuring  
1067 vehicle capacity is never exceeded during either the delivery or pickup phases. We use  $b_i \in \{0, 1\}$   
1068 to indicate whether node  $i$  is a backhaul customer. For VRPB, we require the edge connecting to a  
1069 linehaul customer and a backhaul customer included in the  $E_{\text{unstable}}$ . We employ single hypernode  
1070 aggregation that  $\text{dist}(x_i, \tilde{x}) = \text{dist}(x_i, x_j)$ ,  $\text{dist}(\tilde{x}, x_i) = \text{dist}(x_k, x_i)$ ,  $\tilde{d} = d_j + \dots + d_k$ , and  $\tilde{b} = b_j$   
1071 (we require customer being the same type within each segment that  $b_j = \dots = b_k$ ).

1072 **1-VRPPD.** Compared to the CVRP, the 1-VRPPD (Martinovic et al., 2008) deals with customers  
1073 labeled as either cargo sink ( $d_i < 0$ ) or cargo source ( $d_i > 0$ ), depending on their pickup or delivery  
1074 demand. Along the route of each vehicle, the vehicle could not load negative cargo or cargo exceeding  
1075 the capacity of the vehicle  $C$ . For any segment  $S_{j,k}$ , we define  $D^j = d_j$ ,  $D^{j+1} = d_j + d_{j+1}, \dots$ ,  
1076 and  $D^k = d_j + d_{j+1} + \dots + d_k$ . We further define  $D^{\min} = \min\{0, D_j, D_{j+1}, \dots\}$  and  $D^{\max} =$   
1077  $\max\{0, D_j, D_{j+1}, \dots\}$ . For 1-VRPPD, we require three hypernodes  $\tilde{x}_j = x_j$ ,  $\tilde{x}_{\text{mid}}$ , and  $\tilde{x}_k = x_k$ ,  
1078 where the distances from  $\tilde{x}_{\text{mid}}$  to  $\tilde{x}_j$  or  $\tilde{x}_k$  are 0, and infinity for the other hypernodes. For the  
1079 aggregated demands,  $\tilde{d}_j = D^{\min}$ ,  $\tilde{d}_{\text{mid}} = D^{\max} - D^{\min}$ , and  $\tilde{d}_k = D^k - D^{\max} - D^{\min}$ . Additional  
constraints are added to ensure the directed edges  $\tilde{x}_j \rightarrow \tilde{x}_{\text{mid}} \rightarrow \tilde{x}_k$  are included in the solutions.

1080  
1081 Table 7: Implementation specifications of FSTA hypernode aggregation for CVRP, VRPTW, VRPB  
1082 variants. Refer to Equation 3 for the definitions of  $\tilde{s}_j$ ,  $\tilde{t}_j^l$  and  $\tilde{t}_j^r$ .

| CVRP             |                                    |                   |   |   |
|------------------|------------------------------------|-------------------|---|---|
| Type             | Condition                          | Attribute         | Aggregation   | Additional Constraints / Settings   |
| Two Hypernodes   | Always                             | Location/Distance | $\tilde{x}_j = x_j$<br>$\tilde{x}_k = x_k$  | Include edge $\tilde{x}_j \rightarrow \tilde{x}_k$ in the solution  |
|                  |                                    | Demand            | $\tilde{d}_j = \tilde{d}_k = \frac{1}{2}(d_j + \dots + d_k)$  |   |
| VRPTW            |                                    |                   |   |   |
| Type             | Condition                          | Attribute         | Aggregation   | Additional Constraints / Settings   |
| One Hypernode    | $\tilde{t}_j^l \leq \tilde{t}_j^r$ | Location/Distance | $\text{dist}(x_i, \tilde{x}) = \text{dist}(x_i, x_j)$ ,<br>$\text{dist}(\tilde{x}, x_i) = \text{dist}(x_k, x_i)$                                    | None  |
|                  |                                    | Demand            | $\tilde{d} = d_j + \dots + d_k$   |   |
|                  |                                    | Service Time      | $\tilde{s} = \tilde{s}_j$   |   |
|                  |                                    | Time Windows      | $\tilde{t}^l = \tilde{t}_j^l, \tilde{t}^r = \tilde{t}_j^r$  |   |
| Two Hypernodes   | $\tilde{t}_j^l > \tilde{t}_j^r$    | Location/Distance | $\tilde{x}_j = x_j, \tilde{x}_k = x_k$  | Include edge $\tilde{x}_j \rightarrow \tilde{x}_k$ in solution; set $\text{dist}(\tilde{x}_j, \tilde{x}_k) = 0$ |
|                  |                                    | Demand            | $\tilde{d}_j = \tilde{d}_k = \frac{1}{2}(d_j + \dots + d_k)$  |   |
|                  |                                    | Service Time      | $\tilde{s}_j = 0, \tilde{s}_k = \tilde{s}_j$  |   |
|                  |                                    | Time Windows      | $\tilde{t}_j^l = 0, \tilde{t}_j^r = \tilde{t}_j^l, \tilde{t}_k^l = \tilde{t}_j^l, \tilde{t}_k^r = \infty$   |   |
| VRPB             |                                    |                   |   |   |
| Type             | Condition                          | Attribute         | Aggregation   | Additional Constraints / Settings   |
| One Hypernode    | Always                             | Location/Distance | $\text{dist}(x_i, \tilde{x}) = \text{dist}(x_i, x_j)$ ,<br>$\text{dist}(\tilde{x}, x_i) = \text{dist}(x_k, x_i)$                                    | Require $b_j = \dots = b_k$ (same customer type) during Unstable Edges Detection Stage                          |
|                  |                                    | Demand            | $\tilde{d} = d_j + \dots + d_k$   |   |
|                  |                                    | Is backhaul       | $\tilde{b} = b_j$   |   |
| 1-VRPPD          |                                    |                   |   |   |
| Type             | Condition                          | Attribute         | Aggregation   | Additional Constraints / Settings   |
| Three Hypernodes | Always                             | Location/Distance | $\tilde{x}_j = x_j, \tilde{x}_k = x_k$<br>$\text{dist}(\tilde{x}_j, \tilde{x}_{\text{mid}}) = \text{dist}(\tilde{x}_{\text{mid}}, \tilde{x}_k) = 0$ | Include edges $\tilde{x}_j \rightarrow \tilde{x}_{\text{mid}} \rightarrow \tilde{x}_k$ in the solution          |
|                  |                                    | Demand            | $\tilde{x}_{\text{mid}}$ only connects to $\tilde{x}_j$ and $\tilde{x}_k$   |   |
|                  |                                    |                   | $\tilde{d}_j = D^{\min}, \tilde{d}_{\text{mid}} = D^{\max} - D^{\min},$   |   |
|                  |                                    |                   | $\tilde{d}_k = D^k - D^{\max} - D^{\min}$   |   |

## B.2 PROOF OF FSTA

1112 **Theorem. (Feasibility)** If the aggregated solution  $\tilde{\mathcal{R}}_+$  is a feasible solution to the aggregated problem,  
1113 then  $\mathcal{R}_+$  is a feasible solution to the original, non-aggregated problem. **(Monotonicity)** Let  $\tilde{\mathcal{R}}_+^1$  and  
1114  $\tilde{\mathcal{R}}_+^2$  be two feasible solutions to the aggregated problem, with  $f(\tilde{\mathcal{R}}_+^1) \leq f(\tilde{\mathcal{R}}_+^2)$ , where  $f(\cdot)$  denotes  
1115 the objective function (total travel cost). Then, for the associated solution in the original space, we  
1116 also have  $f(\mathcal{R}_+^1) \leq f(\mathcal{R}_+^2)$ .

1117 **Proof Structure and Notation.** Without loss of generality, we consider a single-route solution  
1118 containing one segment  $S_{j,k} = (x_j \rightarrow \dots \rightarrow x_k)$  with more than one node, i.e., the solution  $\mathcal{R}$   
1119 contains route  $R = (x_0 \rightarrow x_1 \rightarrow \dots \rightarrow S_{j,k} \rightarrow x_{k+1} \rightarrow \dots \rightarrow x_0)$ . We define the aggregated  
1120 problem with node set  $\tilde{V} = \{x_0\} \cup \{x_p\}_{p < j} \cup \{\tilde{S}_{j,k}\} \cup \{x_p\}_{p > k}$ , where nodes outside the segment retain  
1121 their original representation, ensuring their feasibility by construction. Since we enforce the inclusion  
1122 of the edge connecting  $\tilde{x}_j$  and  $\tilde{x}_k$  in dual hypernode aggregation within solution  $\tilde{\mathcal{R}}_+$ , the segment  
1123  $\tilde{S}_{j,k}$  must be incorporated into some route  $\tilde{R}_+^* \in \tilde{\mathcal{R}}_+$  for both hypernode aggregation strategies. We  
1124 denote the improved route containing this segment after mapping back to the original problem as  $R_+^*$ .

1125 We present the segment aggregation strategies for different routing variants below, followed by proofs  
1126 of feasibility and monotonicity for the aggregation scheme. Note that the following analysis naturally  
1127 extends to multi-route solutions with multiple segments per route.

### B.2.1 CVRP

1128 **Aggregation Strategy (Two Hypernodes).** The detailed implementation of FSTA on CVRP can  
1129 be found in Appendix B.1.5 and Table 7. Notice that one single hypernode aggregation is also  
1130 applicatable for CVRP, and  $\tilde{d}_j, \tilde{d}_k$  could take other values as long as  $\tilde{d}_j + \tilde{d}_k = d_j + \dots + d_k$ .

1134 **Feasibility Proof [Capacity Constraint].** Notice that since  $\tilde{d}_j + \tilde{d}_k = d_j + \dots + d_k$ , we have:

$$\begin{aligned} 1136 \quad \sum_{x_i \in \tilde{R}_+^*} d_i &= \sum_{x_i \in \tilde{R}_+^* \setminus \tilde{S}_{j,k}} d_i + \tilde{d}_j + \tilde{d}_k \\ 1137 \quad &= \sum_{x_i \in R_+^* \setminus S_{j,k}} d_i + d_j + \dots + d_k = \sum_{x_i \in R_+^*} d_i \\ 1138 \quad & \\ 1139 \quad & \\ 1140 \quad & \end{aligned} \tag{4}$$

1141 Thus, we have:

$$1143 \quad \sum_{x_i \in \tilde{R}_+^*} d_i \leq C \Rightarrow \sum_{x_i \in R_+^*} d_i \leq C \tag{5}$$

1146 Then, we have a feasible  $\tilde{\mathcal{R}}_+ \Rightarrow$  a feasible  $\mathcal{R}_+$ .

1147  $\square$

1148 **Monotonicity Proof.** Notice that

$$\begin{aligned} 1150 \quad f(\tilde{\mathcal{R}}_+) &= f(\tilde{\mathcal{R}}_+ \setminus \{\tilde{R}_+^*\}) + f(\{\tilde{R}_+^*\}) = f(\mathcal{R}_+ \setminus \{R_+^*\}) + f(\{\tilde{R}_+^*\}) \\ 1151 \quad &= f(\mathcal{R}_+ \setminus \{R_+^*\}) + f(\{R_+^*\}) - \sum_{j \leq q < k} dist(x_q, x_{q+1}) + dist(\tilde{x}_j, \tilde{x}_k) \\ 1152 \quad & \\ 1153 \quad & \\ 1154 \quad & = f(\mathcal{R}_+) + \text{Const}|_{S_{j,k}} \end{aligned} \tag{6}$$

1155 where  $\text{Const}|_{S_{j,k}}$  is a constant once the segment  $S_{j,k}$  is decided. Therefore, we have:

$$1157 \quad f(\tilde{\mathcal{R}}_+^1) \leq f(\tilde{\mathcal{R}}_+^2) \Rightarrow f(\mathcal{R}_+^1) + \text{Const}|_{S_{j,k}} \leq f(\mathcal{R}_+^2) + \text{Const}|_{S_{j,k}} \Rightarrow f(\mathcal{R}_+^1) \leq f(\mathcal{R}_+^2) \tag{7}$$

1159  $\square$

1160 We note that the feasibility proof for capacity constraint and the monotonicity proof could be easily  
1161 extended to the single hypernodes aggregation.

### 1163 B.2.2 VRPTW

1164 **Aggregation Strategy (Mixed Strategies).** The detailed implementation of FSTA on VRPTW can  
1165 be found in Appendix B.1.5 and Table 7. We denote  $s_m^* = s_m + \text{dist}(x_m, x_{m+1})$  for  $j \leq m < k$   
1166 and  $s_k^* = s_k$ . We further set the service time by  $\tilde{s}_m = \sum_{m \leq q \leq k} s_q^*$ , and we repeat the temporal time  
1167 window  $[\tilde{t}_j^l, \tilde{t}_j^r]$  (which could be infeasible) defined by the following recursive relationship:

$$\begin{aligned} 1170 \quad \tilde{t}_m^l &= \begin{cases} t_k^l & m = k \\ \max\{t_m^l, \tilde{t}_{m+1}^l - s_m^*\} & j \leq m \leq k-1, \end{cases} \\ 1171 \quad \tilde{t}_m^r &= \begin{cases} t_k^r & m = k \\ \min\{t_m^r, \tilde{t}_{m+1}^r - s_m^*\} & j \leq m \leq k-1, \end{cases} \end{aligned} \tag{8}$$

1175 where  $[\tilde{t}_m^l, \tilde{t}_m^r]$  is the time window for a node  $x_m$ ,  $s_m$  is the service time at node  $x_m$  and  
1176  $\text{dist}(x_m, x_{m+1})$  is the time to travel from node  $x_m$  to node  $x_{m+1}$ .

1178 **Feasibility Proof [Time Window Constraint].** We first prove for the condition that the temporal time  
1179 window  $[\tilde{t}_j^l, \tilde{t}_j^r]$  is feasible ( $\tilde{t}_j^l < \tilde{t}_j^r$ ) and single hypernode aggregation is applied. Then, we extend to  
1180 the infeasible temporal time window condition where dual hypernode aggregation is applied.

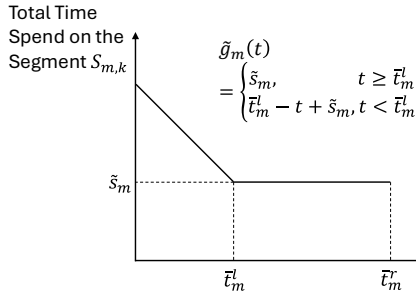
1181 **Condition of Feasible Temporal Time Windows (One Hypernode).** We present an inductive proof  
1182 based on the *segment length*. Given a feasible solution  $\tilde{\mathcal{R}}_+$  for the aggregated problem, we show  
1183 the following two conditions of the corresponding non-aggregated solution  $\mathcal{R}_+$  to satisfy the time  
1184 window constraint:

- 1185 • *Condition (1): We visit each node  $x_m$  before the end of its time window  $t_m^r$ .*
- 1186 • *Condition (2): The total time we spent visiting the entire segment is the same in both  
1187 aggregated and non-aggregated representations.*

1188

1189

1190



1193

1194

1195

1196

1197

1198

1199

1200

1201 Figure 10: This illustration demonstrates the temporal dynamics of the aggregated segment. The left  
 1202 panel shows the time function characterized by a piecewise linear structure: initially decreasing with  
 1203 slope -1, then transitioning to a constant value corresponding to the aggregated left time window  
 1204 boundary. The right panel presents two distinct scenarios that characterize the relationship between  
 1205 the aggregated left time window ( $\tilde{t}_m^l$ ) and the individual non-aggregated left time windows ( $t_m^l$ ).  
 1206

1207 *Proof of Condition (1):*

1208

1209

1210

1211

1212

1213

1214

1215

1216

1217

1218

1219

1220

1221

1222

1223

- *Base case (segment length = 1).* Suppose the segment  $S_{k,k} = (x_k)$  contains a single node  $x_k$ . Then the aggregated problem is identical to the non-aggregated problem by construction, so condition (1) is trivially satisfied.

1224

1225

1226

1227

1228

1229

1230

1231

1232

1233

1234

- *Inductive Step (segment length =  $(k - m) + 1 > 1$ ).* textit the aggregation of the segment  $S_{m+1,k} = (x_{m+1} \rightarrow \dots \rightarrow x_k)$  into  $\tilde{S}_{m+1,k} = \{\tilde{x}_{m+1,k}\}$  satisfies condition (1). We want to show that the aggregation of the segment  $S_{m,k} = (x_m \rightarrow \dots \rightarrow x_k)$  into  $\tilde{S}_{m,k} = \{\tilde{x}_{m,k}\}$  also satisfies condition (1).

Since  $\tilde{\mathcal{R}}_+$  is a feasible solution for the aggregated problem, we will visit the hypernode  $\tilde{x}_{m,k}$  before the end of its time window  $\tilde{t}_m^r = \min\{t_m^r, \tilde{t}_{m+1}^r - s_m^*\}$ . Corresponding, in the associated non-aggregated solution, we visit the node  $x_m$  before its time limit  $t_m^r$ , hence satisfying condition (1) for the node  $x_m$ . Furthermore, in the associated non-aggregated solution, we visit the next node  $x_{m+1}$  before time  $t_m^r + s_m^* \leq \tilde{t}_{m+1}^r$ . Based on the inductive hypothesis, condition (1) holds for the rest of the segment  $(x_{m+1} \rightarrow \dots \rightarrow x_k)$  if we arrive at node  $x_{m+1}$  before its end time. Hence, condition (1) holds for the whole segment  $S_{m,k} = (x_m \rightarrow x_{m+1} \rightarrow \dots \rightarrow x_k)$ .

1235

1236

1237

1238

1239

1240

1241

*Proof of Condition (2):* For all  $m$ , suppose we arrive at the hypernode  $\tilde{x}_{m,k}$  at time  $t \leq \tilde{t}_m^r$  in the aggregated solution. By definition, the total time spent on the aggregated segment (sum of the waiting time, service time, and the travel time) can be written as the following linear function with -1 slope as shown in the first figure in Figure 10.

$$\tilde{g}_m(t) = \begin{cases} \tilde{s}_m, & t \geq \tilde{t}_m^l \\ \tilde{t}_m^l - t + \tilde{s}_m, & t < \tilde{t}_m^l \end{cases} \quad (9)$$

*Note: the first condition  $t \geq \tilde{t}_m^l$  means we do not need to wait at any node in the segment  $S_{m,k}$ , and the second condition means we need to wait at some node in the segment  $S_{m,k}$ .*

It suffices to show that the total time spent on the non-aggregated segment also follows the same function. Again, we prove this by induction.

1242

1243

1244

1245

1246

1247

1248

1249

1250

1251

1252

1253

1254

1255

1256

1257

1258

1259

1260

1261

1262

1263

1264

1265

1266

1267

1268

1269

1270

1271

1272

1273

1274

1275

1276

1277

1278

1279

1280

1281

1282

1283

1284

1285

1286

1287

1288

1289

1290

1291

1292

1293

1294

1295

1296

1297

1298

1299

1300

1301

1302

1303

1304

1305

1306

1307

1308

1309

1310

1311

1312

1313

1314

1315

1316

1317

1318

1319

1320

1321

1322

1323

1324

1325

1326

1327

1328

1329

1330

1331

1332

1333

1334

1335

1336

1337

1338

1339

1340

1341

1342

1343

1344

1345

1346

1347

1348

1349

1350

1351

1352

1353

1354

1355

1356

1357

1358

1359

1360

1361

1362

1363

1364

1365

1366

1367

1368

1369

1370

1371

1372

1373

1374

1375

1376

1377

1378

1379

1380

1381

1382

1383

1384

1385

1386

1387

1388

1389

1390

1391

1392

1393

1394

1395

1396

1397

1398

1399

1400

1401

1402

1403

1404

1405

1406

1407

1408

1409

1410

1411

1412

1413

1414

1415

1416

1417

1418

1419

1420

1421

1422

1423

1424

1425

1426

1427

1428

1429

1430

1431

1432

1433

1434

1435

1436

1437

1438

1439

1440

1441

1442

1443

1445

1446

1447

1448

1449

1450

1451

1452

1453

1454

1455

1456

1457

1458

1459

1460

1461

1462

1463

1464

1465

1466

1467

1468

1469

1470

1471

1472

1473

1474

1475

1242  
1243 We now show the total time function  $g_m(t)$  for the segment  $S_{m,k} = (x_m \rightarrow \dots \rightarrow x_k)$  also  
1244 equals  $\tilde{g}_m(t)$ .  
1245

By definition of the non-aggregated segment, depending on whether we need to wait at the  
1246 first node  $x_m$ , we have:  
1247

$$g_m(t) = \begin{cases} s_m^* + g_{m+1}(t + s_m^*) & t \geq t_m^l \\ t_m^l - t + s_m^* + g_{m+1}(t_m^l + s_m^*) & t < t_m^l. \end{cases} \quad (11)$$

1248  
1249 *Note: the first condition  $t \geq t_m^l$  means we do not need to wait at the first node  $x_m$ , and the  
1250 second condition  $t < t_m^l$  means we need to wait at the first node  $x_m$ .*  
1251

1252 We split the discussion into the following two cases, based on whether we need to wait at  
1253 any node along the segment  $S_{m+1,k}$ , if we leave node  $x_m$  at  $t_m^l$ :

1254 1.  $t_m^l + s_m^* \geq \bar{t}_{m+1}^l$ . In this case,  $t_m^l \geq \bar{t}_{m+1}^l - s_m^*$ , and hence  $\bar{t}_m^l = \max\{t_m^l, \bar{t}_{m+1}^l - s_m^*\} = t_m^l$  as shown in case 1 of Figure 10. Hence, we have  
1255  
1256

$$g_m(t) = \begin{cases} s_m^* + g_{m+1}(t + s_m^*) & t \geq \bar{t}_m^l \\ t_m^l - t + s_m^* + g_{m+1}(t_m^l + s_m^*) & t < \bar{t}_m^l. \end{cases} \quad (12)$$

1257 By inductive hypothesis, we have  
1258  
1259

$$g_{m+1}(t + s_m^*) = \tilde{s}_{m+1}, \quad t \geq t_m^l = \bar{t}_m^l,$$

1260 as in this case  $t + s_m^* \geq t_m^l + s_m^* \geq \bar{t}_{m+1}^l$ .  
1261

1262 Hence, we have  
1263  
1264

$$\begin{aligned} g_m(t) &= \begin{cases} s_m^* + \tilde{s}_{m+1} & t \geq \bar{t}_m^l \\ t_m^l - t + s_m^* + \tilde{s}_{m+1} & t < \bar{t}_m^l. \end{cases} \\ &= \begin{cases} \tilde{s}_m & t \geq \bar{t}_m^l \\ t_m^l - t + \tilde{s}_m & t < \bar{t}_m^l \end{cases} = \tilde{g}_m(t). \end{aligned} \quad (13)$$

1265 where we apply the definition of  $\tilde{s}_m = s_m^* + \tilde{s}_{m+1}$ .  
1266

1267 2.  $t_m^l + s_m^* < \bar{t}_{m+1}^l$ . In this case,  $\bar{t}_{m+1}^l - s_m^* > t_m^l$ , and hence  $\bar{t}_m^l = \max\{t_m^l, \bar{t}_{m+1}^l - s_m^*\} = \bar{t}_{m+1}^l - s_m^*$  as shown in case 2 of Figure 10.  
1268

1269 By inductive hypothesis, we have  
1270  
1271

$$\begin{aligned} g_{m+1}(t_m^l + s_m^*) &= \bar{t}_{m+1}^l - (t_m^l + s_m^*) + \tilde{s}_{m+1} \\ &= \bar{t}_m^l - t_m^l + \tilde{s}_{m+1} \end{aligned} \quad (14)$$

1272 We also have, for all  $t \geq t_m^l$ ,  
1273  
1274

$$\begin{aligned} g_{m+1}(t + s_m^*) &= \begin{cases} \tilde{s}_{m+1}, & t + s_m^* \geq \bar{t}_{m+1}^l \\ \bar{t}_{m+1}^l - (t + s_m^*) + \tilde{s}_{m+1}, & t + s_m^* < \bar{t}_{m+1}^l \end{cases} \\ &= \begin{cases} \tilde{s}_{m+1}, & t \geq \bar{t}_m^l \\ \bar{t}_m^l - t + \tilde{s}_{m+1}, & t_m^l \leq t < \bar{t}_m^l \end{cases} \end{aligned} \quad (15)$$

1275 As a result, we have  
1276  
1277

$$\begin{aligned} g_m(t) &= \begin{cases} s_m^* + \tilde{s}_{m+1} & t \geq \bar{t}_m^l \\ s_m^* + \bar{t}_m^l - t + \tilde{s}_{m+1} & \bar{t}_m^l \leq t < \bar{t}_m^l \\ t_m^l - t + s_m^* + \bar{t}_m^l - t_m^l + \tilde{s}_{m+1} & t < \bar{t}_m^l, \end{cases} \\ &= \begin{cases} \tilde{s}_m & t \geq \bar{t}_m^l \\ \bar{t}_m^l - t + \tilde{s}_m & \bar{t}_m^l \leq t < \bar{t}_m^l \\ \bar{t}_m^l - t + \tilde{s}_m & t < \bar{t}_m^l, \end{cases} \\ &= \begin{cases} \tilde{s}_m & t \geq \bar{t}_m^l \\ \bar{t}_m^l - t + \tilde{s}_m & t < \bar{t}_m^l \end{cases} = \tilde{g}_m(t). \end{aligned} \quad (16)$$

1296 **Condition of Infeasible Temporal Time Windows (Two Hypernodes).** In our time window  
 1297 aggregation,  $\tilde{t}_j^l$  is responsible for the time expenditure and  $\tilde{t}_j^r$  is responsible for feasibility. In this  
 1298 case, we have  $\tilde{t}_j^l > \tilde{t}_j^r$ , which indicates that to maintain feasibility along the segment, one must arrive  
 1299 at the segment before the aggregated start time  $\tilde{t}_j^l$ , and since one arrives earlier, one must wait at  
 1300 some node within the segment. Since  $\tilde{t}_j^l > \tilde{t}_j^r$  is not permitted according to the definition of VRPTW,  
 1301 we then utilize one additional hypernode to increase the representational capacity such that the first  
 1302 hypernode handles the feasibility component ( $\tilde{t}_j^r$ ), and the second hypernode handles the travel time  
 1303 component ( $\tilde{t}_j^l$ ). Specifically,  $\tilde{t}_j^l = 0$ ,  $\tilde{t}_j^r = \tilde{t}_j^r$ ,  $\tilde{t}_k^l = \tilde{t}_j^l$ ,  $\tilde{t}_k^r = \infty$  and  $\tilde{s}_j = 0$ ,  $\tilde{s}_k = \bar{s}_j$  with the  
 1304 additional constraint that  $\text{dist}(\tilde{x}_j, \tilde{x}_k) = 0$ .  
 1305

1306 For time window feasibility (Condition (1)), since  $\tilde{t}_j^r = \bar{t}_j^r$ , the vehicle must serve the segment  
 1307 before  $\bar{t}_j^r$ , ensuring the feasibility of serving each customer in the non-aggregated problem. For  
 1308 travel time equivalence (Condition (2)), the time expended before reaching the second node is  
 1309  $\tilde{s}_j + \text{dist}(\tilde{x}_j, \tilde{x}_k) = 0$ . Namely, after the vehicle arrives at the segment at time  $t$ , the travel time is  
 1310 entirely determined by  $\tilde{t}_k^l = \tilde{t}_j^l$  and  $\tilde{s}_k = \bar{s}_j$ , whereby in the feasible temporal time window situation,  
 1311 the travel time equivalence is demonstrated.  
 1312

1313 We complete the time window constraint feasibility proof for VRPTW for both aggregation strategies  
 1314 across all conditions.  
 1315  $\square$

1316 **Monotonicity Proof.** For the dual hypernode aggregation, please refer to the *Monotonicity Proof* in  
 1317 B.2.1. For the single hypernode aggregation, notice that

$$\begin{aligned} f(\tilde{\mathcal{R}}_+) &= f(\tilde{\mathcal{R}}_+ \setminus \{\tilde{R}_+^*\}) + f(\{\tilde{R}_+^*\}) = f(\mathcal{R}_+ \setminus \{R_+^*\}) + f(\{R_+^*\}) \\ &= f(\mathcal{R}_+ \setminus \{R_+^*\}) + f(\{R_+^*\}) - \sum_{j \leq q < k} \text{dist}(x_q, x_{q+1}) \\ &= f(\mathcal{R}_+) + \text{Const}|_{S_{j,k}} \end{aligned} \quad (17)$$

1323 where  $\text{Const}|_{S_{j,k}}$  is a constant once the segment  $S_{j,k}$  is decided. Therefore, we have:  
 1324

$$f(\tilde{\mathcal{R}}_+^1) \leq f(\tilde{\mathcal{R}}_+^2) \Rightarrow f(\mathcal{R}_+^1) + \text{Const}|_{S_{j,k}} \leq f(\mathcal{R}_+^2) + \text{Const}|_{S_{j,k}} \Rightarrow f(\mathcal{R}_+^1) \leq f(\mathcal{R}_+^2) \quad (18)$$

1326  $\square$

### 1328 B.2.3 VRPB

1330 **Aggregation Strategy (One Hypernode).** The detailed implementation of FSTA on VRPB can be  
 1331 found in Appendix B.1.5 and Table 7.

1332 **Feasibility Proof [Backhaul Constraint].** Without loss of generality, we assume all nodes within the  
 1333 segment  $S_{j,k}$  are backhaul customers ( $b_j = \dots = b_k = 1$ ). Notice that since  $\tilde{d} = d_j + \dots + d_k$ , for  
 1334 the backhaul stage, we have:  
 1335

$$\begin{aligned} \sum_{x_i \in \tilde{R}_+^* \text{ and } b_i=1} d_i &= \sum_{x_i \in \tilde{R}_+^* \setminus S_{j,k} \text{ and } b_i=1} d_i + \tilde{d} \\ &= \sum_{x_i \in R_+^* \setminus S_{j,k} \text{ and } b_i=1} d_i + d_j + \dots + d_k = \sum_{x_i \in R_+^* \text{ and } b_i=1} d_i \end{aligned} \quad (19)$$

1340 For the linehaul stage, we have:  
 1341

$$\sum_{x_i \in \tilde{R}_+^* \text{ and } b_i=0} d_i = \sum_{x_i \in R_+^* \text{ and } b_i=0} d_i \quad (20)$$

1344 Thus, we have:  
 1345

$$\begin{aligned} \sum_{x_i \in \tilde{R}_+^* \text{ and } b_i=0} d_i \leq C &\Rightarrow \sum_{x_i \in R_+^* \text{ and } b_i=0} d_i \leq C \\ \sum_{x_i \in \tilde{R}_+^* \text{ and } b_i=1} d_i \leq C &\Rightarrow \sum_{x_i \in R_+^* \text{ and } b_i=1} d_i \leq C \end{aligned} \quad (21)$$

1350 Then, we have a feasible  $\tilde{\mathcal{R}}_+ \Rightarrow$  a feasible  $\mathcal{R}_+$ .  
 1351  $\square$

1353 **Monotonicity Proof.** Please refer to the monotonicity proof of VRPTW in Appendix B.2.2.  
 1354

1355 B.2.4 1-VRPPD.  
 1356

1357 **Aggregation Strategy (Three Hypernodes).** The detailed implementation of FSTA on 1-VRPPD can  
 1358 be found in Appendix B.1.5 and Table 7.

1359 **Feasibility Proof [1-Commodity Pickup and Delivery Constraint].** A feasible  $\tilde{\mathcal{R}}_+$  indicates that  
 1360 whenever the vehicle is traveling an aggregated segment  $\tilde{S}_{j,k}$ , denoted the starting load of the vehicle  
 1361 to be  $d_{st}$  and ending load of the vehicle to be  $d_{ed}$ , we have:  
 1362

$$\begin{aligned} 1363 \quad 0 &\leq d_{st} + D^{\min} \leq C \\ 1364 \quad 0 &\leq d_{st} + D^{\min} + D^{\max} - D^{\min} \leq C \\ 1365 \end{aligned} \tag{22}$$

1366 which requires  $-D^{\min} \leq d_{st} \leq C - D^{\max}$  and  $d_{ed} = d_{st} + D^k$ .  
 1367

1368 On the other hand, a feasible solution  $\mathcal{R}_+$  indicates that whenever the vehicle is traveling a segment  
 1369  $S_{j,k}$ , denoted the starting load of the vehicle to be  $d_{st}$  and ending load of the vehicle to be  $d_{ed}$ , we  
 1370 have:  
 1371

$$0 \leq d_{st} + D^i \leq C, \quad \forall i \tag{23}$$

1372 which also requires  $-D^{\min} \leq d_{st} \leq C - D^{\max}$  and  $d_{ed} = d_{st} + D^k$ . Then, we have a feasible  $\tilde{\mathcal{R}}_+ \Rightarrow$   
 1373 a feasible  $\mathcal{R}_+$ .  
 1374  $\square$

1375 **Monotonicity Proof.** As  $\text{dist}(\tilde{x}_j, \tilde{x}_{\text{mid}}) = \text{dist}(\tilde{x}_{\text{mid}}, \tilde{x}_k) = 0$ , we can eliminate the middle hypernode  
 1376 and use a two-hypernode representation when calculating the routing objective. Please refer to  
 1377 the monotonicity proof of CVRP in Appendix B.2.1 for the monotonicity proof of two-hypernode  
 1378 representation.  
 1379

1380 C L2SEG DETAILS  
 1381

1383 C.1 COMPARATIVE ANALYSIS OF L2SEG AGAINST EXISTING METHODS  
 1384

1385 **Comparisons with Large Neighborhood Search (LNS).** (1) LNS (Large Neighborhood Search)  
 1386 operates within a bounded local neighborhood. The algorithm selects a specific region, destroys  
 1387 elements within that boundary, and rebuilds only that portion while keeping the rest of the solution  
 1388 intact. For instance, in Li et al. (2021), LNS selects 3-5 subroutes as its neighborhood, modifying  
 1389 only these routes while leaving all others completely unchanged. There is a clear demarcation  
 1390 between the modified neighborhood and the preserved structure. (2) FSTA (our method), in contrast,  
 1391 operates more globally across the entire solution. It can break existing edges and aggregate segments  
 1392 throughout all subroutes simultaneously, without any predefined neighborhood boundaries. The  
 1393 modifications are distributed across the entire solution rather than confined to a local region, which  
 1394 represents a fundamental departure from existing LNS to more efficiently guide the search. We note  
 1395 that such a flexible framework would not be possible without the proposed ML component, which  
 1396 also constitutes the core novelty and contribution of our work to the field. (3) Moreover, FSTA  
 1397 and LNS are complementary: FSTA can be applied on top of LNS, where LNS first selects a large  
 1398 neighborhood, then FSTA fixes stable edges globally within that selected region.

1399 **Comparisons with Evolutionary Algorithms.** L2Seg framework and evolutionary algorithms (Vidal,  
 1400 2022) approach the preservation of solution components from different angles and with distinct  
 1401 goals, and are not interchangeable in use. Evolutionary algorithms (Vidal, 2022) rely on crossover  
 1402 to merge relatively “good” components from different parents, aiming to promote diversity and  
 1403 generate promising offspring, while our L2Seg framework introduces a learning-guided mechanism  
 1404 to detect unstable edges and aggregates stable edge sequences into hypernodes, enabling a new form  
 1405 of segment-based decomposition that improves scalability and efficiency.

1404 **Comparisons with Path Decomposition Method.** (1) Firstly, path decomposition relies on geometric  
 1405 heuristics (e.g., clustering routes by barycenter distances) to identify decomposition boundaries. In  
 1406 contrast, L2Seg employs deep learning models (synergistic NAR-AR architecture) to intelligently  
 1407 predict which segments should be aggregated, capturing complex patterns that simple heuristics  
 1408 cannot identify. We also propose a novel learning-guided framework with bespoke training and  
 1409 inference processes that are unique to the machine learning method. (2) Secondly, while some prior  
 1410 work explores similar decomposition ideas (e.g., on CVRP only), we are the first to study FSTA  
 1411 decomposition theoretically, providing formal definitions, feasibility theorems, and monotonicity  
 1412 guarantees for various VRPs. (3) Lastly, we empirically demonstrate that by leveraging deep learning  
 1413 in our L2Seg framework, our method consistently achieves significant speedups on state-of-the-art  
 1414 backbones. This provides new insights for the community, highlighting the power of learning-guided  
 1415 optimization in accelerating combinatorial solvers.

1416 **Comparisons with Previous Learning-based Framework L2D (Li et al., 2021).** (1) Different  
 1417 from the sub-route level, our method detects unstable edges both within and across sub-routes,  
 1418 enabling more global and flexible decomposition. (2) It optimizes beyond localized neighborhoods  
 1419 by identifying improvements that span multiple distant regions simultaneously. (3) It reduces the size  
 1420 of sub-routes by aggregating stable segments into hypernodes, whereas L2D reduces only the number  
 1421 of sub-routes per iteration. This segment-level aggregation allows more adaptive and coarse-grained  
 1422 reduction, offering higher efficiency and solution quality, while remaining complementary to L2D.

1423 **Comparisons with hypergraph decomposition methods Fu et al. (2023) and Li et al. (2025).** Fu  
 1424 et al. (2023) introduce HDR, a hierarchical destroy-and-repair algorithm that recursively compresses  
 1425 TSP instances to handle problems with millions of cities. While HDR achieves remarkable scalability  
 1426 on very large TSP instances using non-learning heuristics, our approach differs by employing learned  
 1427 policies to identify unstable edges and extending beyond TSP to handle CVRP, VRPTW, and other  
 1428 variants. HDR uses straightforward edge-fixing based on historical local optima, whereas we learn  
 1429 destruction patterns from the lookahead heuristics. Li et al. (2025) propose DRHG, which uses  
 1430 hyper-graphs to reduce consecutive edges and supervised learning for reconstruction. Their approach  
 1431 applies heuristic clustering for destruction followed by ML-based repair of the destroyed segments.  
 1432 Our method takes the opposite approach: we use machine learning to identify unstable edges that  
 1433 should be destroyed, then employ efficient subsolvers for reconstruction. This reversed strategy  
 1434 allows us to leverage learned patterns for the critical decision of what to destroy while using proven  
 1435 optimization techniques for repair. While DRHG demonstrates strong results on TSP and CVRP, our  
 1436 experiments extend to more constrained variants like VRPTW.

## 1437 C.2 INPUT FEATURE DESIGN DETAILS

1439 Previous works Kool et al. (2018); Li et al. (2021); Kwon et al. (2020) typically utilize only basic  
 1440 input features for routing problems (xy-coordinates and normalized demands for node features, and  
 1441 edge cost for edge features). While neural networks can potentially learn complex patterns from these  
 1442 basic features, tailored feature engineering may lead to enhanced model performance. As illustrated  
 1443 in Appendix B.1, we observe that detecting unstable edges may depend on better capturing local  
 1444 dependencies. We therefore design enhanced node and edge features for our learning task, as shown  
 1445 in Table 8. We also include time windows and service time as node features for VRPTWs.

## 1447 C.3 MASKING DETAILS

1449 In general, any set of unstable edges could lead to a feasible FSTA problem reduction. However,  
 1450 employing logic-based local search algorithms to select unstable edges can produce more reasonable  
 1451 action space reduction and improved performance. Thus, we design the deletion and insertion stages  
 1452 of L2Seg to emulate a general local search operation.

1453 **For the deletion stage**, given the current node  $x$ , we mask out nodes that are: (1) not connected to  $x$ ;  
 1454 or (2) part of an edge that has already been deleted during the current deletion stage. Note that the  
 1455 model may select the special ending node  $x_{\text{end}}$  to terminate the decoding sequence.

1456 **For the insertion stage**, given the current node  $x$ , we mask out nodes that are: (1) already connected  
 1457 to  $x$ ; (2) endpoints of two newly inserted edges; or (3) the special ending node  $x_{\text{end}}$ .

1458 Table 8: Description of enhanced input features for nodes and edges.  
1459  
1460

| Type  | Description   | Dimension |
|-------|---|-----------|
| Nodes | The xy coordinates  | 2         |
|       | The normalized demand   | 1         |
|       | The centroid of the subtour for each node   | 2         |
|       | The coordinates of the two nodes connecting to each node                                | 4         |
|       | The travel cost of the two edges connecting to each node                                | 2         |
|       | The relative xy coordinates   | 2         |
|       | The angles w.r.t. the depot   | 1         |
|       | The weighted angles w.r.t. the depot by the distances                                   | 1         |
|       | The distances of the closest 3 neighbor for each node                                   | 3         |
|       | The percentage of the K nearest nodes<br>that are within the same subtour. K=5, 15, 40  | 3         |
| Edges | The percentage of the K% nearest nodes<br>that are within the same subtour. K=5, 15, 40 | 3         |
|       | The travel cost   | 1         |
|       | Whether each edge is within the current solution  | 1         |
|       | The travel cost rank of each edge w.r.t. the corresponding end points                   | 1         |

1479 C.4 TRAINING DATA COLLECTION DETAILS  
1480

1481 In this section, we present pseudocode that demonstrate the process of generating training labels  
1482 for both NAR and AR models in Algorithm 2. As a complement to the methodology described  
1483 in Section 4, we derive our training data from  $N_P$  distinct problem instances and extract labels  
1484 from the first  $T_{IS}$  iterative improvement steps. For the AR labels, which emulate feasible local  
1485 search operations, each label (representing a sequence of nodes) is associated with a quantifiable  
1486 improvement in solution quality. We retain only those labels that yield improvements exceeding the  
1487 threshold  $\eta_{\text{improv}}$ , and we employ stochastic sampling by accepting labels with probability  $\alpha_{AC}$ . This  
1488 selective approach ensures both high-quality training signals and sufficient diversity across problem  
1489 instances and optimization trajectories within the same training budget.

1490 C.5 INFERENCE DETAILS  
1491

1493 In this section, we present the pseudocode that delineates the inference processes of L2Seg-SYN  
1494 (Algorithm 3), L2Seg-NAR (Algorithm 4), and L2Seg-AR (Algorithm 5). It is important to note that  
1495 our implementation leverages batch operations for efficient inference across multiple subproblems  
1496 simultaneously. The K-means clustering algorithm was strategically selected for initial node identifi-  
1497 cation due to its parallelization capabilities. By merging graphs from different subproblems into a  
1498 unified structure, we can execute the clustering algorithm once for the entire problem space. This  
1499 parallel clustering approach through K-means significantly enhances decoding efficiency. Notably,  
1500 within each iterative step, our design requires only a single call of the NAR and AR models, thereby  
1501 optimizing computational resources.

1503 D EXPERIMENTAL AND IMPLEMENTATION DETAILS  
15041505 D.1 BACKBONE SOLVERS  
1506

1507 **LKH-3.** The Lin-Kernighan-Helsgaun algorithm (LKH-3) Helsgaun (2017) represents a strong  
1508 classical heuristic solver for routing problems, which is widely used in NCO for benchmark. It  
1509 employs sophisticated  $k$ -opt moves and effective neighborhood search strategies. For our experiments,  
1510 we impose time limits rather than local search update limits: 150s and 240s for large-capacity CVRP2k  
1511 and CVRP5k, respectively, and 2m, 4m, and 10m for VRPTW1k, VRPTW2k, and VRPTW5k,  
1512 respectively. For small-capacity CVRPs, we adopt the results reported in Zheng et al. (2024).

---

1512  
 1513  
 1514 **Algorithm 2:** Training Data Generation  
 1515 **Input:** Solution distribution  $\mathcal{P}$ , number of instances  $N_{\mathcal{P}}$ , backbone solver  $BS$ , number of  
 1516 iterative steps  $T_{IS}$ , improvement threshold  $\eta_{improv}$ , sample coefficient  $\alpha_{AC}$   
 1517 **Output:** Label sets  $\mathcal{Y}_{NAR}, \mathcal{Y}_{AR}$

1518 1  $\mathcal{Y}_{NAR} \leftarrow \emptyset, \mathcal{Y}_{AR} \leftarrow \emptyset$  **for**  $i \leftarrow 1$  **to**  $N_{\mathcal{P}}$  **do**  
 1519 2     Sample  $P \sim \mathcal{P}$  and obtain an initial solution  $\mathcal{R}$   
 1520 3     **for**  $t \leftarrow 1$  **to**  $T_{IS}$  **do**  
 1521 4          $\mathcal{R}_+ \leftarrow BS(P, \mathcal{R})$  // Apply backbone solver  
 1522 5          $E_{diff} \leftarrow (E_{\mathcal{R}} \setminus E_{\mathcal{R}_+}) \cup (E_{\mathcal{R}_+} \setminus E_{\mathcal{R}})$   
 1523 6          $V_{unstable} \leftarrow V_{E_{diff}}$   
 1524 7          $Y_{NAR}^P \leftarrow \mathbb{1}\{x \in V_{unstable}\}$  // NAR model labels  
 1525 8          $\mathcal{Y}_{NAR} \leftarrow \mathcal{Y}_{NAR} \cup \{(P, Y_{NAR}^P)\}$   
 1526 9          $\mathcal{K}_{TR} \leftarrow DFS(P, V_{unstable}, E_{diff})$  // Find sequences  
 1527 10         **foreach**  $K \in \mathcal{K}_{TR}$  **do**  
 1528 11             Obtain  $P_K$  with solution  $R_K$  and sequence  $y_K$  with Improvement  
 1529 12             **if**  $Improvement \geq \eta_{improv}$  and with probability  $\alpha_{AC}$  **then**  
 1530 13                  $\mathcal{Y}_{AR} \leftarrow \mathcal{Y}_{AR} \cup \{(P_K, y_K)\}$  // AR model labels  
 1531 14             **end if**  
 1532 15                 // Skip sequences with low improvement or by  
 1533 16                 probability  
 1534 17         **end foreach**  
 1535 18          $\mathcal{R} \leftarrow \mathcal{R}_+$  // Update current solution  
 1536 19     **end for**  
 1537 20     **return**  $\mathcal{Y}_{NAR}, \mathcal{Y}_{AR}$

---



---

1538  
 1539  
 1540  
 1541 **Algorithm 3:** L2Seg-SYN: Synergized Prediction  
 1542 **Input:** Problem  $P$ , current solution  $\mathcal{R}$ , NAR model, AR model, threshold  $\eta$ , number of clusters  
 1543  $n_{KMEANS}$   
 1544 **Output:** Set of unstable edges  $E_{unstable}$

1545 1  $\mathcal{P}_{TR} \leftarrow \text{DecomposeIntoSubproblems}(P, \mathcal{R})$  // Partition into  $\sim |\mathcal{R}|$   
 1546 subproblems  
 1547 2  $E_{unstable} \leftarrow \emptyset$   
 1548 3 **for** each subproblem  $P_{TR} \in \mathcal{P}_{TR}$  **do**  
 1549 4      $\mathbf{p}^{NAR} \leftarrow \text{NARModel}(P_{TR})$  // Get NAR predictions for each node  
 1550 5      $\hat{y}_{NAR} \leftarrow \{x_i \mid p_i^{NAR} \geq \eta\}$  // Identify unstable nodes via threshold  
 1551 6     Clusters  $\leftarrow \text{KMeans}(\hat{y}_{NAR}, n_{KMEANS})$  // Group unstable nodes into  
 1552 clusters  
 1553 7     InitialNodes  $\leftarrow \{x \mid x = \arg \max_{x_i \in c} p_i^{NAR}, c \in \text{Clusters}\}$   
 1554 8         // Select initial node with highest probability for the AR  
 1555 model  
 1556 9      $E_{unstable}^{P_{TR}} \leftarrow \emptyset$  // Unstable edges for this subproblem  
 1557 10     **for** each node  $x_{init} \in \text{InitialNodes}$  with corresponding  $P_{TR}$  **do**  
 1558 11          $E_{x_{init}}^{P_{TR}} \leftarrow \text{ARModel}(P_{TR}, x_{init})$  // Get unstable edges via the AR  
 1559 model  
 1560 12          $E_{unstable}^{P_{TR}} \leftarrow E_{unstable}^{P_{TR}} \cup E_{x_{init}}^{P_{TR}}$   
 1561 13     **end for**  
 1562 14      $E_{unstable} \leftarrow E_{unstable} \cup E_{x_{init}}^{P_{TR}}$  // Aggregate unstable edges  
 1563 15     **end for**  
 1564 16     **return**  $E_{unstable}$

---

1566  
1567  
1568  
1569  
1570

---

**Algorithm 4:** L2Seg-NAR: Non-Autoregressive Prediction

---

1571 **Input:** Problem  $P$ , current solution  $\mathcal{R}$ , NAR model, threshold  $\eta$   
 1572 **Output:** Set of unstable edges  $E_{\text{unstable}}$

1573 1  $\mathcal{P}_{\text{TR}} \leftarrow \text{DecomposeIntoSubproblems}(P, \mathcal{R})$  // Partition into  $\sim |\mathcal{R}|$   
 1574    subproblems

1575 2  $E_{\text{unstable}} \leftarrow \emptyset$

1576 3 **for** each subproblem  $P_{\text{TR}} \in \mathcal{P}_{\text{TR}}$  **do**

1577    4  $\mathbf{p}^{\text{NAR}} \leftarrow \text{NARModel}(P_{\text{TR}})$  // Get NAR predictions for each node

1578    5  $\hat{y}_{\text{NAR}} \leftarrow \{x_i \mid p_i^{\text{NAR}} \geq \eta\}$  // Identify unstable nodes via threshold

1579    6  $E_{\text{unstable}}^{P_{\text{TR}}} \leftarrow \{(x_i, x_j) \mid x_i \in \hat{y}_{\text{NAR}} \text{ or } x_j \in \hat{y}_{\text{NAR}}, \text{ and } (x_i, x_j) \in E_{P_{\text{TR}}}\}$   
     // Mark all edges connected to the unstable nodes as  
     unstable

1580    7  $E_{\text{unstable}} \leftarrow E_{\text{unstable}} \cup E_{\text{unstable}}^{P_{\text{TR}}}$  // Aggregate unstable edges

1581 8 **end for**

1582 9 **return**  $E_{\text{unstable}}$

---

1586  
1587  
1588  
1589  
1590  
1591  
1592  
1593  
1594

---

**Algorithm 5:** L2Seg-AR: Autoregressive Prediction

---

1595 **Input:** Problem  $P$ , current solution  $\mathcal{R}$ , AR model, number of clusters  $n_{\text{KMEANS}}$   
 1596 **Output:** Set of unstable edges  $E_{\text{unstable}}$

1597 1  $\mathcal{P}_{\text{TR}} \leftarrow \text{DecomposeIntoSubproblems}(P, \mathcal{R})$  // Partition into  $\sim |\mathcal{R}|$   
 1598    subproblems

1599 2  $E_{\text{unstable}} \leftarrow \emptyset$

1600 3 **for** each subproblem  $P_{\text{TR}} \in \mathcal{P}_{\text{TR}}$  **do**

1601    4 Clusters  $\leftarrow \text{KMeans}(\text{AllNodes in } P_{\text{TR}}, n_{\text{KMEANS}})$  // Cluster all nodes

1602    5 Centroids  $\leftarrow \{\text{ComputeCentroid}(c) \mid c \in \text{Clusters}\}$

1603    6 InitialNodes  $\leftarrow \{x \mid x = \arg \min_{x_i \in c} \text{Distance}(x_i, \text{centroid}_c), c \in \text{Clusters}\}$   
     // Select node closest to each cluster centroid for the AR  
     model

1604    7  $E_{\text{unstable}}^{P_{\text{TR}}} \leftarrow \emptyset$  // Unstable edges for this subproblem

1605    8 **for** each node  $x_{\text{init}} \in \text{InitialNodes}$  with corresponding  $P_{\text{TR}}$  **do**

1606      9  $E_{x_{\text{init}}}^{P_{\text{TR}}} \leftarrow \text{ARModel}(P_{\text{TR}}, x_{\text{init}})$  // Get unstable edges via the AR  
       model

1607      10  $E_{\text{unstable}}^{P_{\text{TR}}} \leftarrow E_{\text{unstable}}^{P_{\text{TR}}} \cup E_{x_{\text{init}}}^{P_{\text{TR}}}$

1608    11 **end for**

1609    12  $E_{\text{unstable}} \leftarrow E_{\text{unstable}} \cup E_{\text{unstable}}^{P_{\text{TR}}}$  // Aggregate unstable edges

1610 13 **end for**

1611 14 **return**  $E_{\text{unstable}}$

---

1616  
1617  
1618  
1619

1620 **LNS.** Local Neighborhood Search (LNS) Shaw (1998) is a powerful decomposition-based metaheuristic  
 1621 that iteratively improves solutions by destructively and constructively exploring defined search  
 1622 neighborhoods. We implement LNS following the approach in Li et al. (2021), where neighborhoods  
 1623 consisting of three adjacent subroutes are randomly selected for re-optimization. We establish time  
 1624 limits of 150s and 240s for large-capacity CVRP2k and CVRP5k, respectively; 2.5m, 4m, and 5m for  
 1625 small-capacity CVRP1k, CVRP2k, and CVRP5k, respectively; and 2m, 4m, and 10m for VRPTW1k,  
 1626 VRPTW2k, and VRPTW5k, respectively. LKH-3 serves as the backbone solver with a 1,000 per-step  
 1627 local search updates limit.

1628 **L2D.** Learning to Delegate (L2D) Li et al. (2021) is the state-of-the-art learning-based optimization  
 1629 framework that integrates neural networks with classical optimization solvers to intelligently delegate  
 1630 subproblems to appropriate solvers. The framework employs a neural network trained to identify the  
 1631 most promising neighborhoods for improvement. For comparative fairness, we apply identical time  
 1632 limits and backbone solver configurations as used in our LNS implementation. When augmented by  
 1633 L2Seg, training proceeds in two stages: we first train the L2D models following the methodology in  
 1634 Li et al. (2021), then train the L2Seg model using the resulting pre-trained L2D models.

1635 **Initial Solution Heuristics.** For both training data generation and inference, we employ the initial  
 1636 solution heuristic inspired by (Li et al., 2021). Our method partitions nodes according to their angular  
 1637 coordinates with respect to the depot. We begin by selecting a reference node, marking its angle as  
 1638 0, and incrementally incorporate additional nodes into the same group until the collective demand  
 1639 approaches the capacity threshold ( $c_{\text{init}} K_{\text{veh}} C \approx \sum d_i$ ), where approximately  $K_{\text{veh}}$  vehicles would  
 1640 be required to service the group. This process continues sequentially, forming new groups until all  
 1641 customers are assigned. Finally, we apply LKH-3 in parallel to solve each subproblem independently.  
 1642 In our implementation, we set  $K_{\text{veh}} = 6$  and  $\alpha_{\text{init}} = 0.95$  as the controlling parameters.

## 1643 D.2 BASELINES

1644 In this section, we provide further clarification regarding the baselines used in our comparative  
 1645 analysis, beyond the backbone solvers. We independently executed LKH-3, LNS, and L2D using  
 1646 consistent parameters. Results for SIL were sourced from Luo et al. (2024), L2R from Zhou et al.  
 1647 (2025a), and all other baselines from Zheng et al. (2024). When multiple variants of a baseline were  
 1648 presented in the original publications, we selected the configuration that achieved the best objective  
 1649 values. Since the original implementation of NDS (Hottung et al., 2025) was evaluated on NVIDIA  
 1650 A100 GPUs whereas our experiments use NVIDIA V100 GPUs, we re-ran NDS on our hardware for  
 1651 fair comparison.

1652 It is important to note that all reported results were evaluated on identical test instances (for CVRPs) or  
 1653 on instances sampled from the same distribution (for VRPTWs), ensuring fair comparison. Moreover,  
 1654 our experiments were conducted on hardware with less powerful GPUs compared to those utilized in  
 1655 Luo et al. (2024); Zheng et al. (2024); Zhou et al. (2025a). This hardware discrepancy suggests that  
 1656 the performance advantages demonstrated by our proposed model would likely persist or potentially  
 1657 increase if all methods were evaluated on identical computing infrastructure.

1658 We re-implemented the backbone solvers and L2D (Li et al., 2021) to ensure a fair and strong  
 1659 comparison. Notably, prior studies (Zheng et al., 2024; Ye et al., 2024) did not explore configurations  
 1660 optimized for L2D’s full potential. Specifically, they imposed overly conservative limits (e.g., only  
 1661 allowing 1 trail) on LKH-3 local search updates and did not supply current solution information to  
 1662 the LKH-3 solver during the resolution process. This significantly weakened L2D’s performance in  
 1663 their benchmarks. In contrast, our comparison reflects L2D’s best achievable performance.

## 1664 D.3 PARAMETERS AND TRAINING HYPERPARAMETERS

1665 **Parameters.** Table 9 lists the values of parameters used in training data generation and inference.  
 1666 **Training Hyperparameters.** For model training, we optimize both NAR and AR architectures using  
 1667 the ADAM optimizer with a consistent batch size of 128 across 200 epochs for all problem variants.  
 1668 The learning rate is calibrated at  $10^{-3}$  for large-capacity CVRPs and  $10^{-4}$  for small-capacity CVRPs  
 1669 and VRPTWs. The loss function employs weighted components with  $w_{\text{pos}} = 9$ ,  $w_{\text{insert}} = 0.8$ , and  
 1670  $w_{\text{delete}} = 0.2$ . All computational experiments are conducted on a single NVIDIA V100 GPU, with  
 1671 training duration ranging from approximately 0.5 to 1.5 days, scaling with problem dimensionality.

1674 Table 9: A list of parameters and their values used in our experiments for training and inference.  
1675  
1676

| Training Data Generation                                 |   |
|--|---|
| Parameter  | Value   |
| # of instances $N_P$                                     | 1000  |
| # of iterative steps $T_{IS}$                            | 40  |
| Improvement threshold $\eta_{\text{improv}}$             | 0   |
| Sample coefficient $\alpha_{AC}$                         | 0 for small-capacity CVRPs and VRPTWs<br>0.4 for large-capacity CVRPs   |
| Inference  |   |
| Parameter  | Value   |
| Threshold $\eta$ for NAR model                           | 0.6   |
| # of K-MEANS clusters $n_{\text{KMEANS}}$                | 3   |
| # of LKH-3 local search updates limit per iterative step | 1000  |
| Solve time limits  | 150s, 240s for large-capacity CVRP2k, 5k<br>2.5m, 4m, 5m for small-capacity CVRP1k, 2k, 5k<br>2m, 4m, 10m for VRPTW1k, 2k, 5k |

1693  
1694 Regarding network architecture, our encoder maps node features  $\mathbf{X} \in \mathbb{R}^{n \times 25}$  for standard problems  
1695 ( $\mathbf{X} \in \mathbb{R}^{n \times 28}$  for VRPTWs) to node embeddings via  $\mathbf{h}_i^{\text{init}} = \text{Concat}(\mathbf{h}_i^{\text{MLP}}, \mathbf{h}_i^{\text{POS}}) \in \mathbb{R}^{2d_h}$ , where  
1696  $d_h = 128$ . They then undergo processing through  $L_{\text{TFM}} = 2$  Transformer layers (Vaswani, 2017)  
1697 with route-specific attention masks, followed by a Graph Attention Network to derive the final  
1698 node embeddings  $\mathbf{H}^{\text{GNN}}$ . The transformer implementation utilizes 2 attention heads, 0.1 dropout  
1699 regularization, ReLU activation functions, layer normalization, and feedforward dimensionality of  
1700 512. Our GNN employs a transformer convolution architecture with 2 layers ( $L_{\text{GNN}} = 2$ ) and a single  
1701 attention head.

1702 Supplementary to the specifications in Section 4, we delineate additional hyperparameters for our  
1703 decoder modules. The NAR decoder computes  $\mathbf{p}^{\text{NAR}}$  (node instability probabilities) via an MLP  
1704 with sigmoid activation for final probability distribution. The AR decoder incorporates single-layer  
1705 Gated Recurrent Units (GRUs), complemented by a single-layer/single-head transformer for the  
1706 deletion mechanism and a four-layer/single-head transformer for the insertion procedure.

1707 All the training hyperparameters are summarized in Table 10.

#### 1709 D.4 INSTANCE GENERATION

1711 In general, we generate all training and test instances following established methodologies: Zheng  
1712 et al. (Zheng et al., 2024) for CVRP and Solomon (Solomon, 1987) for VRPTW. Specifically, For  
1713 small-capacity CVRPs, nodes are uniformly distributed within the  $[0, 1]$  square, with integer demands  
1714 ranging from 1 to 9 (inclusive). Vehicle capacities are set to  $C = 200, 300$ , and 300 for problem  
1715 sizes 1k, 2k, and 5k, respectively. For large-capacity CVRPs, we maintain identical configurations  
1716 except for increased vehicle capacities of  $C = 500$  and 1000 for CVRP1k and CVRP5k, respectively.  
1717 For VRPTWs, we adopt the same spatial distribution, demand structure, and capacity constraints as  
1718 the small-capacity CVRPs. Service times are uniformly set to 0.2 time units for each customer and  
1719 0 for the depot. Time windows are generated according to the methodology outlined in Solomon  
1720 (Solomon, 1987).

1721 Our experimental framework comprises distinct datasets for training, validation, and testing:

- 1723 • **Training:** 1,000 instances for each problem type and scale to generate training labels
- 1724 • **Validation:** 30 instances per problem configuration
- 1725 • **Testing:** For small-capacity CVRPs, we utilize the 1,000 test instances from Zheng et al.  
1726 (Zheng et al., 2024); for large-capacity CVRPs and VRPTWs, we evaluate on 100 instances  
1727 sampled from the same distribution as the training data

1728 Table 10: A list of hyperparameters and their values used in our model architecture and training.  
1729  
1730

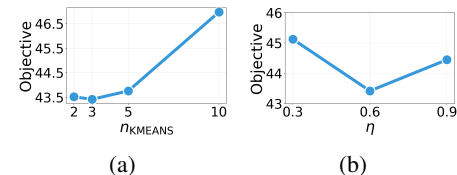
| Training Configuration                                   |   |
|--|---|
| Parameter  | Value   |
| Optimizer  | ADAM  |
| Batch size   | 128   |
| # of epochs  | 200   |
| Learning rates   | $10^{-3}$ for large-capacity CVRPs<br>$10^{-4}$ for small-capacity CVRPs and VRPTWs |
| Weight of unstable nodes $w_{\text{pos}}$                | 9   |
| Weight of prediction in insert stage $w_{\text{insert}}$ | 0.8   |
| Weight of prediction in delete stage $w_{\text{delete}}$ | 0.2   |
| Computing Resource                                       | Single NVIDIA V100 GPU  |
| Model Architecture                                       |   |
| Parameter  | Value   |
| Hidden dimension   | 128   |
| <b>Encoder Transformer</b>                               |   |
| # of layers $L_{\text{TFM}}$                             | 2   |
| # of attention heads                                     | 2   |
| Dropout regularization                                   | 0.1   |
| Activation function                                      | ReLU  |
| Feedforward dimension                                    | 512   |
| Normalization  | Layer normalization   |
| <b>Encoder GNN</b>                                       |   |
| Architecture   | Transformer Convolution Network   |
| # of layers $L_{\text{GNN}}$                             | 2   |
| # of attention heads                                     | 1   |
| <b>Decoder Components</b>                                |   |
| NAR decoder activation function                          | Sigmoid   |
| # of layers in GRUs                                      | 1   |
| <b>AR Transformer in Deletion Stage</b>                  |   |
| # of layers $L_{\text{delete}}^{\text{MHA}}$             | 1   |
| # of attention heads                                     | 1   |
| <b>AR Transformer in Insertion Stage</b>                 |   |
| # of layers $L_{\text{insert}}^{\text{MHA}}$             | 4   |
| # of attention heads                                     | 1   |

1764  
1765 E ADDITIONAL EXPERIMENTS AND ANALYSIS  
17661767 E.1 HYPERPARAMETER STUDY  
1768

1769 Figure 11 depicts the effects of  $n_{\text{KMEANS}}$  and  $\eta$ . We  
1770 observe that the best performance is when  $n_{\text{KMEANS}} = 3$   
1771 and  $\eta = 0.6$ , suggesting that designating a moderate pro-  
1772 portion of edges as unstable represents the most effective  
1773 strategy.

1775 E.2 RESULTS ON REALISTIC ROUTING DATASETS  
1776

1777 We further evaluate L2Seg on the CVRPLib realis-  
1778 tic routing dataset (Uchoa et al., 2017; Arnold et al.,  
1779 2019), adhering to the settings established in Zheng et al.  
1780 (2024), which incorporates instances from CVRP Set-X [54] and the very large-scale CVRP dataset  
1781 Set-XXL in the test set. The instances within CVRPLib exhibit more realistic spatial distributions  
(distinct from simplistic uniform or clustered patterns), greater diversity, and better representation of

1774  
1775 Figure 11: Analysis of key hyperparam-  
1776 eters: (a) number of clusters  $n_{\text{MEANS}}$ , and  
1777 (b) balancing factor  $\eta$ .  
1778

real-world logistical challenges. For this evaluation, we employ models trained on synthetic small-capacity CVRP2k and CVRP5k datasets and zero-shot transfer them to CVRPLib. Time constraints of 240s and 600s are implemented for L2Seg during testing. Additional methodological details are provided in Appendix D. As demonstrated in Table 11, LNS augmented with L2Seg-*SYN* surpasses all other learning-based methods in performance. Significantly, the computational time required by LNS+L2Seg-*SYN* (600s) is substantially less than that of the previously best-performing learning-based model, UDC- $x_{250}$ . These results further substantiate L2Seg’s exceptional generalizability across varied problem distributions.

Table 11: CVRPLib results. We present the gap to the best known solutions (%).

| Dataset, $N \in$       | LEHD       | ELG aug $\times 8$ | GLOP-LKH3                    | TAM(LKH3)                    |
|------------------------|------------|--------------------|------------------------------|------------------------------|
| Set-X,(500,1,000]      | 17.4%      | 7.8%               | 16.8%                        | 9.9%                         |
| Set-XXL,(1,000,10,000] | 22.2%      | 15.2%              | 19.1%                        | 20.4%                        |
| Dataset, $N \in$       | UDC- $x_2$ | UDC- $x_{250}$     | LNS+L2Seg- <i>SYN</i> (240s) | LNS+L2Seg- <i>SYN</i> (600s) |
| Set-X,(500,1,000]      | 16.5%      | 7.1%               | 7.5%                         | 6.9%                         |
| Set-XXL,(1,000,10,000] | 31.3%      | 13.2 %             | 12.5%                        | 12.0%                        |

### E.3 RESULTS ON CLUSTERED CVRP AND HETEROGENEOUS-DEMAND CVRP

Table 12: Results on clustered CVRP and heterogeneous-demand CVRP. We present gains to the backbone solver LNS and the performance of LKH-3 for reference.

| Methods                                     | Clustered CVRP2k     |                 |                   | Clustered CVRP5k     |                 |                   |
|---|----------------------|-----------------|-------------------|----------------------|-----------------|-------------------|
|   | Obj. $\downarrow$    | Gain $\uparrow$ | Time $\downarrow$ | Obj. $\downarrow$    | Gain $\uparrow$ | Time $\downarrow$ |
| LKH-3 (Helsgaun, 2017) (for reference)      | 42.06                | -               | 150s              | 62.33                | -               | 240s              |
| LNS (Shaw, 1998)                            | 41.54                | 0.00%           | 150s              | 61.42                | 0.00%           | 240s              |
| L2Seg- <i>SYN</i> -LNS (zero-shot transfer) | 41.03                | 1.23%           | 150s              | 60.87                | 0.90%           | 240s              |
| L2Seg- <i>SYN</i> -LNS                      | <b>40.73</b>         | <b>1.95%</b>    | 150s              | <b>60.11</b>         | <b>2.13%</b>    | 240s              |
| Methods                                     | Hetero-demand CVRP2k |                 |                   | Hetero-demand CVRP5k |                 |                   |
|   | Obj. $\downarrow$    | Gain $\uparrow$ | Time $\downarrow$ | Obj. $\downarrow$    | Gain $\uparrow$ | Time $\downarrow$ |
| LKH-3 (Helsgaun, 2017) (for reference)      | 46.02                | -               | 150s              | 65.89                | -               | 240s              |
| LNS (Shaw, 1998)                            | 45.77                | 0.00%           | 150s              | 64.81                | 0.00%           | 240s              |
| L2Seg- <i>SYN</i> -LNS (zero-shot transfer) | 44.35                | 3.10%           | 150s              | 64.28                | 0.82%           | 240s              |
| L2Seg- <i>SYN</i> -LNS                      | <b>44.15</b>         | <b>3.54%</b>    | 150s              | <b>64.15</b>         | <b>1.02%</b>    | 240s              |

To demonstrate L2Seg’s robustness across diverse and more realistic scenarios beyond uniform distributions, we provide in-distribution and zero-shot generalization evaluation of our L2Seg on instances with different customer and demand distributions.

Following Li et al. (2021), we generate clustered CVRP instances with 7 clusters. For heterogeneous-demand scenarios, we employ a skewed distribution where high and low demands ( $d \in \{1, 2, 8, 9\}$ ) occur with probability 0.2 each, while others ( $d \in \{3, 4, 5, 6, 7\}$ ) occur with probability 0.04 each. All experiments use LNS as the backbone solver, with LKH-3 included for reference.

Table 12 presents the comprehensive results. L2Seg demonstrates consistent improvements across all settings: zero-shot transfer achieves 1.23% to 3.10% gains over LNS, while in-distribution testing reaches 1.02% to 3.54% improvements depending on problem size and variant. These experiments demonstrate that L2Seg maintains consistent improvements across diverse real-world conditions, from uniform spatial layouts to clustered distributions and heterogeneous demands.

### E.4 STANDARD DEVIATION COMPARISON

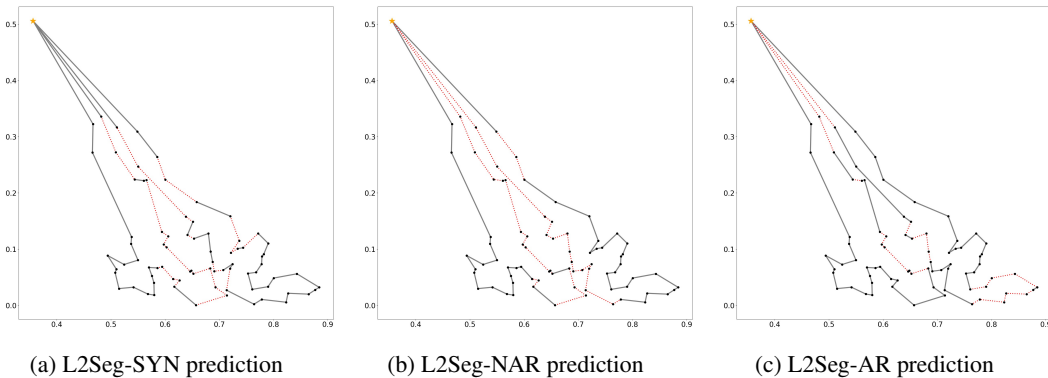
In this section, we provide standard deviation statistics for L2Seg-*SYN* across three different backbone solvers on large-capacity CVRPs. We conduct 5 independent trials using different random seeds for each method. All experiments are terminated at the specified time limit, and we report the standard deviations of the objective values for all 6 methods. The results are presented in Table 13. While

1836 LKH-3 exhibits the lowest variance among baseline methods, our L2Seg approach also demonstrates  
 1837 consistently low variance across different problem types and backbone solvers, confirming both the  
 1838 effectiveness and stability of our method.  
 1839

1840 Table 13: Performance comparison of backbone solvers with and without L2Seg-SYN on large-scale  
 1841 CVRP instances. Results represent mean objective values  $\pm$  standard deviation across 5 independent  
 1842 trials of testing. L2Seg-SYN demonstrates consistent performance improvements with low variance,  
 1843 indicating both effectiveness and stability of the approach.  
 1844

| 1846 | Methods               | CVRP2k            |                 |                   | CVRP5k            |                 |                   |
|------|-----------------------|-------------------|-----------------|-------------------|-------------------|-----------------|-------------------|
|      |                       | Obj. $\downarrow$ | Gain $\uparrow$ | Time $\downarrow$ | Obj. $\downarrow$ | Gain $\uparrow$ | Time $\downarrow$ |
| 1848 | LKH-3 Helsgaun (2017) | 45.24 $\pm$ 0.17  | 0.00%           | 152s              | 65.34 $\pm$ 0.29  | 0.00%           | 242s              |
| 1849 | LKH+L2Seg-SYN         | 43.92 $\pm$ 0.20  | 2.92%           | 152s              | 64.12 $\pm$ 0.34  | 1.87%           | 248s              |
| 1850 | LNS Shaw (1998)       | 44.92 $\pm$ 0.24  | 0.00%           | 154s              | 64.69 $\pm$ 0.37  | 0.00%           | 246s              |
| 1851 | LNS+L2Seg-SYN         | 43.42 $\pm$ 0.22  | 3.34%           | 152s              | 63.94 $\pm$ 0.35  | 1.16%           | 241s              |
| 1852 | L2D Li et al. (2021)  | 43.69 $\pm$ 0.21  | 0.00%           | 153s              | 64.21 $\pm$ 0.32  | 0.00%           | 243s              |
| 1853 | L2D+L2Seg-SYN         | 43.35 $\pm$ 0.23  | 0.78%           | 157s              | 63.89 $\pm$ 0.34  | 0.50%           | 248s              |

## 1854 E.5 CASE STUDY: COMPARISON OF PREDICTIONS OF THREE L2SEG APPROACHES



1867 Figure 12: Prediction comparison of L2Seg-SYN, L2Seg-NAR, and L2Seg-AR on two adjacent  
 1868 routes from a small-capacity CVRP1k solution. Red dashed lines indicate predicted unstable edges.  
 1869 L2Seg-SYN provides the most reasonable predictions, while L2Seg-NAR over-predicts unstable  
 1870 edges and L2Seg-AR fails to identify unstable regions.  
 1871

1872 We present a case study on a small-capacity CVRP1k instance to analyze model prediction behavior.  
 1873 Since the learned model ultimately predicts on two adjacent routes, we visualize unstable edge  
 1874 predictions (red dashed lines) for two such routes using L2Seg-SYN, L2Seg-NAR, and L2Seg-AR in  
 1875 Figure 12. L2Seg-SYN demonstrates selective prediction behavior, avoiding boundary edges while  
 1876 targeting specific unstable edges within route interiors—a pattern consistent with our observations  
 1877 in Appendix B.1.1. L2Seg-NAR successfully identifies unstable regions (route interiors) but lacks  
 1878 discrimination, predicting nearly all edges within these regions as unstable without capturing local  
 1879 dependencies. L2Seg-AR exhibits selective prediction within regions but fails to properly identify  
 1880 unstable regions, as many predictions occur at boundaries. These results provide insight into  
 1881 L2Seg-SYN’s hybrid approach: the NAR component first identifies unstable regions, while the AR  
 1882 component leverages local information to make accurate predictions within each identified region.  
 1883

## 1884 E.6 UNSTABLE AND STABLE EDGES CONVERGENCE

1885 We conducted experiments measuring overlapping predicted edges between adjacent iterations over  
 1886 the first 10 rounds, revealing interesting dynamics: The overlap of predicted unstable edges increases  
 1887 from 28% to 54%, while stable edge overlap increases from 47% to 69% across iterations, shown in  
 1888

Table 14: Unstable and stable edges convergence at the first 10 iterations

| Round #                              | 1     | 2     | 3     | 5     | 7     | 9     |
|--------------------------------------|-------|-------|-------|-------|-------|-------|
| Unstable Edge Overlapping Percentage | 28.2% | 33.5% | 41.2% | 49.2% | 48.8% | 54.1% |
| Stable Edge Overlapping Percentage   | 47.2% | 58.2% | 60.5% | 64.7% | 67.3% | 69.4% |
| Avg Segment Length                   | 2.45  | 2.57  | 2.44  | 3.04  | 2.87  | 2.73  |

the Table 14. This indicates gradual but not rapid convergence, allowing our method to continuously explore new regions for re-optimization rather than getting trapped in fixed segments.

### E.7 THE NEURAL NETWORK OVERHEADS OF L2SEG

We measured the overhead across CVRP and VRPTW instances ranging from 1k to 5k nodes in the Table 15. Even with our most complex model (L2Seg-SYN), the overhead consistently remains below 10% of the total iteration time (ranging from 7.2% to 9.6%). This indicates that the overhead scales efficiently and predictably. Generally speaking, the overhead primarily stems from neural network inference, which is driven by two factors: input data size and network call frequency. Regarding the former, L2Seg employs a Batched Sub-Route Processing design. During embedding, we split problems into adjacent route pairs and use batch processing. This avoids memory bottlenecks and ensures that inference time scales efficiently for large-scale cases. Regarding the latter, the frequency of calling L2Seg is a tunable hyperparameter.

Table 15: Computational overhead analysis of L2Seg variants across problem scales

| Method        | CVRP1k              |                     |               | CVRP2k              |                     |               | CVRP5k              |                     |               |
|---------------|---------------------|---------------------|---------------|---------------------|---------------------|---------------|---------------------|---------------------|---------------|
|               | Avg L2Seg Time/Iter | Avg Total Time/Iter | Overhead Rate | Avg L2Seg Time/Iter | Avg Total Time/Iter | Overhead Rate | Avg L2Seg Time/Iter | Avg Total Time/Iter | Overhead Rate |
| L2Seg-NAR-LNS | 0.38s               | 8.4s                | 4.5%          | 0.62s               | 11.4s               | 5.4%          | 0.80s               | 12.9s               | 6.2%          |
| L2Seg-AR-LNS  | 0.63s               | 9.8s                | 6.4%          | 0.90s               | 10.8s               | 8.3%          | 1.24s               | 13.9s               | 8.9%          |
| L2Seg-SYN-LNS | 0.76s               | 10.5s               | 7.2%          | 1.14s               | 12.5s               | 9.1%          | 1.33s               | 14.1s               | 9.4%          |
| VRPTW1k       |                     |                     |               | VRPTW2k             |                     |               | VRPTW5k             |                     |               |
| L2Seg-NAR-LNS | 0.37s               | 8.9s                | 4.2%          | 0.61s               | 10.4s               | 5.9%          | 0.83s               | 12.8s               | 6.5%          |
| L2Seg-AR-LNS  | 0.62s               | 9.1s                | 6.8%          | 0.96s               | 11.9s               | 8.1%          | 1.14s               | 12.4s               | 9.2%          |
| L2Seg-SYN-LNS | 0.76s               | 10.1s               | 7.5%          | 0.97s               | 10.8s               | 9.0%          | 1.36s               | 14.2s               | 9.6%          |

### E.8 TIME OF TRAINING L2SEG

We give the time spent on data collection, training the NAR, AR, and total time when training L2Seg. Empirically, our training pipeline scales efficiently, requiring under 3 days for CVRP5k. We project that scaling to 10k instances would take approximately 6 days, which is still feasible.

Table 16: Training time breakdown for L2Seg across problem scales

|        | Data Collection | Training time NAR | Training time AR | Total (parallel) |
|--------|-----------------|-------------------|------------------|------------------|
| CVRP1k | 6.3h            | 6.8h              | 13.7h            | 20.0h            |
| CVRP2k | 10.4h           | 10.4h             | 22.4h            | 32.8h            |
| CVRP5k | 19.2h           | 18.1h             | 40.7h            | 59.9h            |

## F BROADER IMPACTS

On one hand, the integration of deep learning into discrete optimization offers promising advances for real-world domains such as public logistics and transportation systems, where additional considerations for social equity and environmental sustainability can be incorporated. On the other

1944 hand, the application of deep learning methodologies in discrete optimization necessitates substantial  
1945 computational resources for model training, potentially leading to increased energy consumption and  
1946 carbon emissions. The quantification and mitigation of these environmental impacts represent critical  
1947 areas for ongoing research and responsible implementation.

1948

1949

## 1950 G LARGE LANGUAGE MODELS USAGE

1951 We used LLMs to assist with manuscript revision. After completing the initial draft without LLM  
1952 assistance, we consulted LLMs for suggestions on improving specific text passages. All LLM-  
1953 generated advice was carefully reviewed to ensure accuracy before incorporation. LLMs were not  
1954 used for research tasks or any purpose beyond text refinement.

1955

1956

1957

1958

1959

1960

1961

1962

1963

1964

1965

1966

1967

1968

1969

1970

1971

1972

1973

1974

1975

1976

1977

1978

1979

1980

1981

1982

1983

1984

1985

1986

1987

1988

1989

1990

1991

1992

1993

1994

1995

1996

1997